Excitation of Surface Phonon-Polariton Wavesat Interface of a Gold Thin Film and a Columnar Silicon Carbide Thin Film

Emadoddin Yaghooti* and Ferydon Babaei

Department of Physics, University of Qom, Qom, Iran

Corresponding author email: e.yaghooti@stu.qom.ac.ir

Received: Mar. 9, 2025, Revised: Oct. 29, 2025, Accepted: Nov. 17, 2025, Available Online: Nov. 19, 2025.
DOI: Will be added soon.

Abstract—In this study, optical modeling of surface phonon-polariton excitation at the interface of a metal thin film and a dielectric columnar thin film in the Kretschmann configuration was investigated using the transfer matrix method. The model solves the curl Maxwell's equations with appropriate boundary conditions. Surface phonon-polaritons are a type of surface electromagnetic waves arising from the coupling between polarized photons and optical phonons in polar dielectrics. In polar dielectrics, there exists a narrow energy range, known as the Reststrahlen band, where these waves cannot propagate due to variations in the refractive index. Within this region, the coupling between optical phonons and polarized photons is enhanced. The excitation of surface phonon-polariton modes can extend across a wide frequency range, from the infrared to the terahertz region, depending on the structural configuration. The Structural and optical parameters, as well as the longitudinal and transverse optical frequencies, on the reflection dips in the metal-dielectric reflection spectra and the Reststrahlen bandwidth, was calculated and analyzed. Surface phonon-polariton excitation offers a wide range of applications in data storage, thermal emission, and metamaterials.

Keywords: Columnar Thin Film, Reststrahlen Band, Surface Phonon-Polaritons, Transfer Matrix.

I. INTRODUCTION

The study of surface electromagnetic waves at the interface of a metal thin film and a dielectric columnar thin film has garnered significant attention from researchers [1]-[5]. Given that only a few materials support the propagation of surface phonon-polariton (SPhP) waves, exploring this topic from various dimensions can lead to fascinating scientific insights. The excitation of surface phonon-polariton modes holds potential applications in data storage [6], optical waveguides [7],[8], advanced sensors [9], thermal emission [10], and metamaterials [11].

The internal energy of a solid resides in the vibrations of its constituent particles. These vibrations can be decomposed into components along orthogonal axes, where each particle can be classically modeled as three harmonic oscillators. Collective harmonic oscillations of all atoms in a crystalline structure are called "phonons", which are quantized energy packets of these vibrations. Phonons are characterized by their vibrational frequency ω, and the vibrations on the surface can be modeled as a linear chain of atoms, with dynamical equations derived based on the nearest-neighbor approximation. Solving these equations yields two solutions for ω; the optical branch frequency (ω_+) and the acoustic branch frequency (ω_-). Thus, the phonon dispersion diagram consists of two branches. Acoustic modes are represented as longitudinal acoustic (LA) or transverse acoustic (TA), while optical modes are referred to as longitudinal optical (LO) or transverse optical (TO). In the optical branch, adjacent atoms oscillate in opposite phases, whereas in the acoustic branch, neighboring atoms oscillate in phase. For instance, Rayleigh waves, a type of surface acoustic wave, propagate on the surface of solids both longitudinally and transversely,

decaying exponentially with distance from the surface [12].

Polariton is a general term describing the coupled state of a polarized photon excitation. It represents a quasi-particle arising from the coupling of electromagnetic waves with vibrational excitations in the crystal lattice [13]. Surface phonon-polaritons (SPhPs) result from the interaction of electromagnetic waves with optical lattice vibrations (phonons). This coupling typically occurs in polar crystals in the mid-infrared to terahertz range, leading to the excitation of SPhPs. Optical phonons are vibrational modes in crystals that result from atoms in the primitive cell moving in opposite directions, coupling with electromagnetic radiation [14]. Compared to acoustic phonons, they typically carry greater energy and can be examined with infrared and Raman spectroscopy [15]. These modes significantly influence a material's dielectric and optical behavior, particularly in insulators and semiconductors. In polar materials, coupling between optical phonons and the electric field gives rise to effects such as LO-TO splitting and distinctive lattice dynamics [16].

SPhPs are generated at the interface of metals with high carrier density, like gold and silver, and polar dielectrics with minimal optical losses, in the mid-infrared to terahertz range. The propagation of SPhPs at the interface between the dielectric and the metal decays exponentially with distance from the interface. This exponential decay prevents the momentum of the incident light from matching the phonon momentum [17],[18]. The Reststrahlen band is an infrared range where polar crystals exhibit strong phonon–photon coupling, producing very high reflectivity and effectively acting as a mirror between the transverse optical (TO) and longitudinal optical (LO) phonon frequencies [19]. This effect stems from the ionic crystal's dielectric response, in which optical lattice vibrations interact with electromagnetic waves. In polar materials, the dielectric function shows a pole-like behavior near the TO and LO frequencies, resulting in a pronounced Reststrahlen effect where waves within this band are largely reflected with little transmission [20]. The exact location and width of the band are set by the material's lattice dynamics, including ionic masses, bond strengths, and crystal symmetry, and the Reststrahlen region is widely used in infrared optics for coatings, filters, and spectroscopy [21]. Beyond this band, the material becomes more transparent as the dielectric response weakens and transmission increases.

To excite SPhPs, this momentum mismatch must be compensated. In phononic environments, momentum enhancement of incident light is achieved using configurations such as the Kretschmann setup. In this setup, light is incident from a dielectric medium (e.g., a prism) at an angle larger than the critical angle onto a metal thin film. Total internal reflection occurs, and the incident photon's wave vector matches that of the surface phonons at the metal-phononic interface via tunneling, facilitating coupling and excitation of SPhPs. This results in a sharp dip in the reflection spectrum, indicating SPHP excitation [2],[22].

At lower frequencies, below the mid-infrared range, plasmonic response weakens or disappears entirely. Given that SPhPs are excited in the mid-infrared and that electromagnetic coupling in polar dielectrics occurs within this frequency range, they are utilized in applications such as nanolithography, near-field optical microscopy, spectroscopy, and biosensors. Infrared detectors are another potential application, divided into two types: thermal and photonic detectors [6]. Thermal infrared detectors operate based on conductivity changes induced by infrared heating but suffer from slow response and low detection accuracy. Photonic infrared detectors, on the other hand, offer fast response, high sensitivity, and accurate detection, working with light sources associated with free charges [23].

The columnar thin films are a two-dimensional class of sculptured thin films. Sculptured thin films (STFs) act as anisotropic and uniaxial heterogeneous media in the visible and infrared ranges, as their voids are smaller than the wavelength of visible light. Structural

parameters of STFs vary based on the method of their fabrication. One such method is oblique angle deposition, where physical vapor deposition with anisotropic growth modulation produces columnar thin films [24]-[26].

In this study, the propagation of SPhPs at the planar interface between a Gold thin film and a columnar silicon carbide thin film was examined in the Kretschmann configuration by transfer matrix method. The effects of structural parameters, including the growth angle of nanocolumns (x), the thickness of the gold thin film (d_{met}), the thickness of the silicon carbide thin film (d_{disc}), and the azimuthal angle of the incident light (θ), on SPhP propagation were analyzed. The prism used was borosilicate glass (BK7) with a refractive index of n=1.52, while the porosity (air volume fraction) of silicon carbide varied from 0.2 to 0.8. For each porosity value, reflectance intensity spectra for p-polarized incident light under varying structural and optical parameters were plotted as a function of wavelength, and SPhP excitation mechanisms were analyzed (Fig. 1).

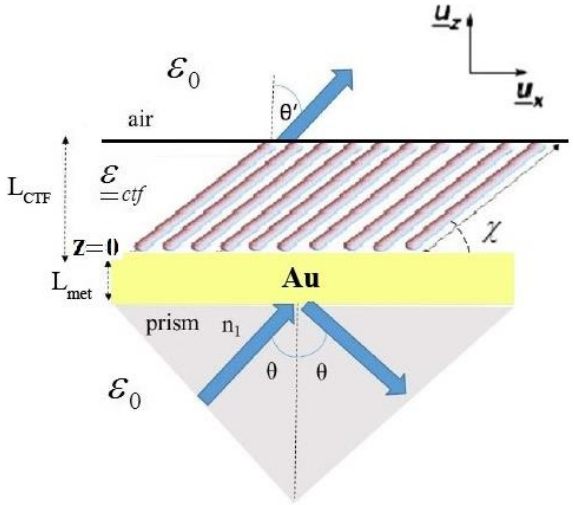

Fig. 1. A schematic of the proposed structure for the excitation of surface phonon-polariton waves in the Kretschmann configuration.

II. THEORETICAL FRAMEWORK

Reststrahlen Band is a significant concept in the field of solid-state physics and optics, commonly addressed in studies involving light scattering, particularly Raman scattering. The Reststrahlen band refers to the range of energy or shifted frequencies resulting from the interaction of light with phonons (lattice vibrations) in materials. In other words, this band represents the energy transfer between photons (light) and phonons during the scattering process [27]. In a crystalline medium, photons alter their energy and momentum due to interactions with lattice vibrations (phonons). These changes can be categorized into two types [28]. *Stokes Scattering*: The photon transfers a portion of its energy to the lattice, generating a phonon. *Anti-Stokes Scattering*: The photon absorbs energy from an existing phonon in the lattice, resulting in an increase in its energy.

The Reststrahlen band corresponds to the energy difference between the scattered photon and the incident photon, which equals the phonon energy. Accordingly, when light strikes the interface of a metal and a dielectric, it expands its energy to excite surface waves. For this to occur, the light must pass through a prism with a real and positive permittivity before reaching the metal-dielectric interface, providing the energy required for excitation [29].

The interaction of phonons and electromagnetic waves can be described using Maxwell's equations. For a plane wave with a wave vector $\boldsymbol{\kappa}$ in a charge-free medium, the governing equations are:

$$\nabla \cdot \mathbf{D} = 0 \tag{1}$$

$$\varepsilon(\omega)(\boldsymbol{\kappa} \cdot \mathbf{E}) = 0 \tag{2}$$

where, $\mathbf{D}$ is the electric displacement vector and $\mathbf{E}$ is the electric field vector.

To establish the above relations, there are two possible approaches:

$$\varepsilon(\omega) = 0 \tag{3}$$

Or:

$$(\boldsymbol{\kappa} \cdot \mathbf{E}) = 0 \tag{4}$$

The first solution corresponds to the longitudinal mode, with the longitudinal resonance frequency $\omega = \omega_L$. The second solution corresponds to the transverse mode, representing the transverse resonance frequency $\omega = \omega_T$. Using Maxwell's equations, the dispersion relation for the phonon-polariton is derived as follows [30]:

$$\kappa^2 = \varepsilon(\omega)\frac{\omega^2}{c^2} \tag{5}$$

where c is the speed of photons in a vacuum and $\varepsilon(\omega)$ is the dielectric function of the material, expressed as [31]:

$$\varepsilon(\omega) = \varepsilon(\infty)\frac{\omega_L^2 - \omega^2}{\omega_T^2 - \omega^2} \tag{6}$$

where $\omega(\infty)$ is the high-frequency dielectric constant and represents the contribution of bound-electron polarizability to the permittivity, providing the background screening of ionic motion and thus setting the photonic asymptote of $\varepsilon(\omega)$. From solving the above equation for the phonon-polariton dispersion relation, we obtained [32]:

$$\omega^2 = \frac{1}{2\varepsilon_\infty}\left[c^2\kappa^2 - \varepsilon_\infty\omega_L^2 \pm \sqrt{\left(c^2\kappa^2 + \varepsilon_\infty\omega_L^2\right)^2 - s}\right] \tag{7}$$

Here $s = 4c^2k^2\varepsilon_\infty\omega_T^2$ denotes the discriminant appearing under the square root. The phonon-polariton dispersion curve will consist of two branches: the lower and upper branches.

In Fig. 2, the behavior of the dielectric function of a phononic and polar dielectric environment, $\varepsilon(\omega)$, is plotted as a function of frequency. It is clearly observed that the dielectric function is positive when the frequency is lower than ω_T and below ω_L. Therefore, the electromagnetic wave can propagate in the material. For frequencies between ω_T and ω_L, the dielectric function is negative, and the electromagnetic wave cannot propagate and exponentially decays. This region is called the Reststrahlen band. When a plane wave with the corresponding frequency passes through the Reststrahlen band at the surface of a polar dielectric crystal, positive ions move in the direction of the field, and negative ions move in the opposite direction. As a result, the real part of the dielectric function is negative, and a decaying field is generated in the polar dielectric crystal. This decaying field is known as surface polariton-phonons.

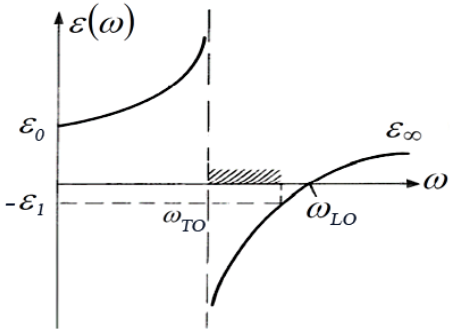

Fig. 2. The behavior of the dielectric function of a phononic environment and a polar dielectric [32].

Using Maxwell's equations, the dispersion relation for surface polariton-phonons can be obtained as follows:

$$\varepsilon(\omega)\sqrt{\kappa^2 - \frac{\omega^2}{c^2}} = -\sqrt{\kappa^2 - \varepsilon(\omega)\frac{\omega^2}{c^2}} \tag{8}$$

$$\omega = c\kappa\sqrt{\frac{1+\varepsilon(\omega)}{\varepsilon(\omega)}} \tag{9}$$

The above equation lies within the frequency range between the transverse and longitudinal frequencies because the dielectric function is negative in this range.

III. OPTICAL MODELING

Based on the structure studied in this research (Fig. 1), the sculptured region, consisting of silicon carbide columns, represents a porous nanostructured medium where the pore sizes and column diameters are smaller than the wavelengths of visible and infrared light. To address this, a process is needed to treat the nanostructured medium as a microstructure medium. This homogenization process transforms the heterogeneous and anisotropic medium into a homogeneous one, effectively

converting the porous material-air mixture into a continuous medium [25].

The metallic thin film is bounded on one side by a phononic medium with a lower refractive index and on the other side by a dielectric (a prism) with a higher refractive index, forming a Kretschmann configuration (see Fig. 1). The amplitudes of transmitted and reflected waves are connected to the incident amplitudes via a transfer matrix. Energy conservation is then applied to compute optical absorption, which reveals the excitation of surface phonon-polariton waves. The Bruggeman homogenization formalism and the transfer matrix method are described in the following sections.

A. *Bruggeman Homogenization Formalism*

In the Bruggeman homogenization Formalism, each column is considered as a chain of identical ellipsoids with negligible interactions. This approach is used to obtain the permittivity tensor of the composite medium (deposited material and vacuum) [25,33].

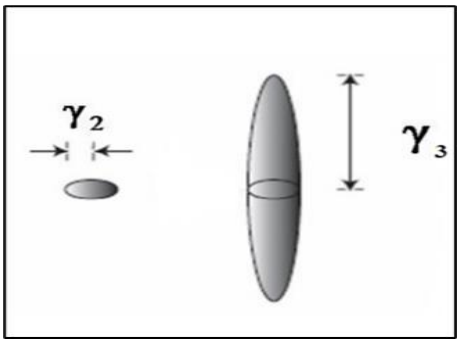

Fig. 3. A representation of ellipsoids.

These ellipsoids have three semi-axes a, b, and c, and the equation of an ellipsoid is as follows:

$$\frac{x^2}{a^2}+\frac{y^2}{b^2}+\frac{z^2}{c^2}=1 \tag{10}$$

The cross-section of each ellipsoid is assumed to be circular, so one of the axes is considered as a unit, and the other two are calculated relative to it. The ratios of the semi-axes, which are now dimensionless, are represented by γ_3 and γ_2. Here, γ_3 indicates the length of the ellipsoid, while γ_2 represents its width. Additionally, it is always assumed that $\gamma_3 > \gamma_2$. The surface of each ellipsoid relative to its center in the Cartesian coordinate system is described by the equation [34]:

$$x^2+\left(\frac{y}{\gamma_2}\right)^2+\left(\frac{z}{\gamma_3}\right)^2=\delta^2 \tag{11}$$

The permittivity is assigned to each of the coordinate axes. Thus, for the *x*, *y*, and *z* directions, the permittivity is represented by ε_a, ε_b, and ε_c, respectively. The reference permittivity tensor can be expressed as follows [35]:

$$\varepsilon_{ref}=\begin{bmatrix}\varepsilon_a & 0 & 0\\ 0 & \varepsilon_b & 0\\ 0 & 0 & \varepsilon_c\end{bmatrix} \tag{12}$$

On the other hand:

$$f_s+f_v=1 \tag{13}$$

it represents the sum of the volume fractions of the material (f_s) and the vacuum (f_v).

According to Bruggeman's theory, we have [36]:

$$f_s \underline{\underline{a}}_s + f_v \underline{\underline{a}}_v = \underline{\underline{0}} \tag{14}$$

wherer a_v is the polarizability tensor of the vacuum, and a_s is the polarizability tensor of the material [37].

$$\underline{\underline{a}}_{s,v}=\varepsilon_0\left(\varepsilon_{s,v}\underline{\underline{I}}-\underline{\underline{\varepsilon}}_{ref}\right).\left[\underline{\underline{I}}+i\omega\varepsilon_0\underline{\underline{D}}_{s,v}.\left(\varepsilon_{s,v}\underline{\underline{I}}-\underline{\underline{\varepsilon}}_{ref}\right)\right]^{-1} \tag{15}$$

where $D_{s,v}$ is the depolarization tensor of the ellipsoids representing the deposited material and the vacuum, which is defined as follows [38]:

$$D_{s,v} = \frac{-i}{4\pi\omega\varepsilon_0}\int_0^{2\pi} d\varphi \int_0^{\pi} d\theta \sin\theta \cdot \frac{\left(\frac{\cos\theta}{\gamma^3}\right)^2 \mathbf{U}_z\mathbf{U}_z \sin^2\theta\left[\cos^2\varphi \mathbf{U}_x\mathbf{U}_x + \left(\frac{\sin\varphi}{\gamma^2}\right)^2 \mathbf{U}_y\mathbf{U}_y\right]}{\varepsilon_a\left(\frac{\cos\theta}{\gamma^3}\right)^2 + \sin^2\theta\left[\varepsilon_b\cos^2\varphi + \varepsilon_c\left(\frac{\sin\varphi}{\gamma^2}\right)^2\right]} \tag{16}$$

where θ and φ are the azimuthal and polar angles, $\varepsilon_{s,v}$ is the relative permittivity of the deposited material and the vacuum, and $\underline{\underline{\mathbf{I}}}$ is the identity tensor. ε_{ref} represents the relative permittivity of the homogenized medium in the reference state, assuming the axes of the ellipsoids are aligned parallel to the Cartesian coordinate axes. It is expressed as follows:

$$\underline{\underline{\varepsilon}}_{ref} = \varepsilon_a \hat{\mathbf{u}}_x\hat{\mathbf{u}}_x + \varepsilon_b \hat{\mathbf{u}}_y\hat{\mathbf{u}}_y + \varepsilon_c \hat{\mathbf{u}}_c\hat{\mathbf{u}}_c \tag{17}$$

where $\mathbf{u_x}$, $\mathbf{u_y}$, and $\mathbf{u_z}$ represent the orientation vectors along the *x*, *y*, and *z*-axes, respectively. By applying boundary conditions and using iterative methods, such as the Jacobi iteration, the relative permittivity of the homogenized composite material can be obtained as follows [39]:

$$\varepsilon_{ref}^{[n]} = u\left[\varepsilon_{ref}^{[n-1]}\right] \tag{18}$$

$$\varepsilon_{ref}^{[0]} = I\left[f\varepsilon_s + (1-f)\varepsilon_v\right] \tag{19}$$

The Jacobi operator matrix is defined as follows:

$$u\left[\varepsilon_{ref}\right] = \frac{\frac{f\varepsilon_s}{I + i\omega\varepsilon_0 D_s\left(\varepsilon_s I - \varepsilon_{ref}\right)} + \frac{(1-f)\varepsilon_v}{I + i\omega\varepsilon_0 D_v\left(\varepsilon_v I - \varepsilon_{ref}\right)}}{\frac{f}{I + i\omega\varepsilon_0 D_s\left(\varepsilon_s I - \varepsilon_{ref}\right)} + \frac{(1-f)}{I + i\omega\varepsilon_0 D_v\left(\varepsilon_v I - \varepsilon_{ref}\right)}} \tag{20}$$

If the norm of the Jacobi operator matrix is less than one, the iterative process converges, yielding the values of ε_a, ε_b, and ε_c. Finally, the relative permittivity ε_{ref} is determined [40].

B. *Transfer Matrix Method*

After obtaining the relative permittivity, the principal permittivity of the porous medium (the columnar silicon carbide dielectric thin film) is calculated using rotation as follows [41]:

$$\underline{\underline{\varepsilon}}_{CTF} = \underline{\underline{S}}_y(\chi)\cdot\underline{\underline{\varepsilon}}_{ref}\cdot\underline{\underline{S}}_y^{\dagger}(\chi) \tag{21}$$

where χ is the growth angle of the nanocolumns, and the tilted tensor $\underline{\underline{S}}_y(\chi)$ is defined as follows [42]:

$$\underline{\underline{S}}_y(\chi) = \hat{\mathbf{u}}_y\hat{\mathbf{u}}_y + \left(\hat{\mathbf{u}}_x\hat{\mathbf{u}}_x + \hat{\mathbf{u}}_z\hat{\mathbf{u}}_z\right)\cos\chi + \left(\hat{\mathbf{u}}_z\hat{\mathbf{u}}_x - \hat{\mathbf{u}}_x\hat{\mathbf{u}}_z\right)\sin\chi \tag{22}$$

To study light propagation in the structure, Maxwell's curl equations must be solved. Subsequently, the transfer matrix method is applied to solve these equations for the phononic medium, the metallic medium, and the vacuum. This approach allows for the determination of the electric and magnetic field components.

1. Transfer matrix of the phononic medium

Considering the structural relations for a dielectric columnar thin film (phononic medium), we have the following [2]:

$$\mathbf{D}(\mathbf{r},\omega) = \varepsilon_0\underline{\underline{S}}_y(\chi)\cdot\underline{\underline{\varepsilon}}_{ref}^{0}(\omega)\cdot\underline{\underline{S}}_y^{\dagger}(\chi)\cdot\mathbf{E}(\mathbf{r},\omega) \tag{23}$$

$$\mathbf{B}(\mathbf{r},\omega) = \mu_0\mathbf{H}(\mathbf{r},\omega) \tag{24}$$

where the electric and magnetic fields are expressed as follows:

$$\mathbf{E}(\mathbf{r},\omega) = \mathbf{e}(z,\kappa,\psi,\omega)\exp\left[i\kappa\left(x\cos\psi + y\sin\psi\right)\right] \tag{25}$$

$$\mathbf{H}(\mathbf{r},\omega) = \mathbf{h}(z,\kappa,\psi,\omega)\exp\left[i\kappa\left(x\cos\psi + y\sin\psi\right)\right] \tag{26}$$

where $\kappa = k_0 \sin\theta$, k_0 is the vacuum wave number, and θ and ψ are the polar and azimuthal angles, respectively. Maxwell's curl equations, in the absence of charge and current sources, are given as follows [1]:

$$\nabla \times \mathbf{E}(\mathbf{r},\omega) = i\omega \mathbf{B}(\mathbf{r},\omega) \tag{27}$$

$$\nabla \times \mathbf{H}(\mathbf{r},\omega) = -i\omega \mathbf{D}(\mathbf{r},\omega) \tag{28}$$

The electric and magnetic fields from equations (25) and (26) can be rewritten as follows:

$$\mathbf{E}(\mathbf{r},\omega) = \left(\hat{\mathbf{u}}_{\mathbf{x}} e_x + \hat{\mathbf{u}}_{\mathbf{y}} e_y + \hat{\mathbf{u}}_{\mathbf{z}} e_z\right) \exp\left[i\kappa\left(x\cos\psi + y\sin\psi\right)\right] \tag{29}$$

$$\mathbf{H}(\mathbf{r},\omega) = \left(\hat{\mathbf{u}}_{\mathbf{x}} h_x + \hat{\mathbf{u}}_{\mathbf{y}} h_y + \hat{\mathbf{u}}_{\mathbf{z}} h_z\right) \exp\left[i\kappa\left(x\cos\psi + y\sin\psi\right)\right] \tag{30}$$

By equating the coefficients of the unit vector components in the structural relations, the components of the electric and magnetic fields can be determined.

Using equation (27) for the $\hat{\mathbf{u}}_x$ component, we have [25]:

$$i\kappa e_z \sin\psi - \frac{de_z}{dz} = i\omega\mu_0 h_x \tag{31}$$

And for the $\hat{\mathbf{u}}_y$ component, we have:

$$\frac{de_x}{dz} - i\kappa e_z \cos\psi = i\omega\mu_0 h_y \tag{32}$$

And similarly, for the $\hat{\mathbf{u}}_{\mathbf{z}}$ component, we have:

$$\kappa\left(e_y \cos\psi - e_x \sin\psi\right) = \omega\mu_0 h_z \tag{33}$$

Using equation (28) for the $\hat{\mathbf{u}}_x$ component, we have [43]:

$$i\kappa h_z \sin\psi - \frac{dh_y}{dz} = -i\omega\varepsilon_0 \left\{ e_x\left(\varepsilon_b \cos^2\chi + \varepsilon_a \sin^2\chi\right) + e_z\left(\varepsilon_b \cos\chi \sin\chi - \varepsilon_a \sin\chi\cos\chi\right)\right\} \tag{34}$$

And for the $\hat{\mathbf{u}}_y$ component, we have:

$$\frac{dh_x}{dz} - i\kappa h_z \cos\psi = -i\omega\varepsilon_0 e_y \tag{35}$$

And also, for the $\hat{\mathbf{u}}_{\mathbf{z}}$ component, we have:

$$i\kappa(h_y \cos\psi - h_x \sin\psi) = -i\omega\varepsilon_0 \left\{ e_x\left(\varepsilon_b \cos\chi \sin\chi - \varepsilon_a \sin\chi\cos\chi\right) + e_z\left(\varepsilon_b \cos^2\chi + \varepsilon_a \sin^2\chi\right)\right\} \tag{36}$$

Using equations (31) to (36), the z-components of the electric and magnetic fields are obtained as follows [25]:

$$e_z(z,\kappa,\psi,\omega) = \frac{\varepsilon_d(\omega)}{\varepsilon_a(\omega)\varepsilon_b(\omega)} \times \times e_x(z,\kappa,\psi,\omega)\left[\varepsilon_a(\omega) - \varepsilon_b(\omega)\right]\sin\chi\cos\chi + + \frac{\kappa}{\omega\varepsilon_0} e_x(z,\kappa,\psi,\omega)\left[h_x(z,\kappa,\psi,\omega)\sin\psi - - h_y(z,\kappa,\psi,\omega)\cos\psi\right] \tag{37}$$

$$h_z(z,\kappa,\psi,\omega) = -\frac{\kappa}{\omega\mu_0} \times \times \left[e_x(z,\kappa,\psi,\omega)\sin\psi - e_y(z,\kappa,\psi,\omega)\cos\psi\right] \tag{38}$$

In the above equations, ε_d is the scalar relative permittivity of the composite medium [37].

$$\varepsilon_d(\omega) = \frac{\varepsilon_a(\omega)\varepsilon_b(\omega)}{\varepsilon_a(\omega)\cos^2\chi + \varepsilon_b(\omega)\sin^2\chi} \tag{39}$$

By eliminating e_z and h_z from the above equations, a matrix equation is obtained as follows [25]:

$$\frac{d}{dz}\left[\underline{f}(z,\kappa,\psi,\omega)\right] = i\left[\underline{\underline{P}}(\kappa,\psi,\omega)\right]\left[\underline{f}(z,\kappa,\psi,\omega)\right] \tag{40}$$

where:

$$\left[\underline{f}(z,\kappa,\psi)\right]=\begin{bmatrix} e_x(z,\kappa,\psi,\omega) \\ e_z(z,\kappa,\psi,\omega) \\ h_x(z,\kappa,\psi,\omega) \\ h_y(z,\kappa,\psi,\omega) \end{bmatrix} \quad (41)$$

where $\left[\underline{f}(z,k,\psi)\right]$ is a column matrix, and $\left[\underline{\underline{P}}(\kappa,\psi,)\right]$ is a 4×4 kernel matrix, expressed as follows [43]:

$$\left[\underline{\underline{P}}(\kappa,\psi)\right]=\begin{bmatrix} 0 & 0 & 0 & \omega\mu_0 \\ 0 & 0 & -\omega\mu_0 & 0 \\ 0 & -\omega\varepsilon_0\varepsilon_c & 0 & 0 \\ \omega\varepsilon_0\varepsilon_d & 0 & 0 & 0 \end{bmatrix}+$$
$$+\frac{\kappa\varepsilon_d(\varepsilon_a-\varepsilon_b)}{\varepsilon_a\varepsilon_b}\sin\chi\cos\chi\begin{bmatrix} \cos\psi & 0 & 0 & 0 \\ \sin\psi & 0 & 0 & 0 \\ 0 & 0 & 0 & 0 \\ 0 & 0 & -\sin\psi & \cos\psi \end{bmatrix}+$$
$$+\frac{\kappa^2}{\omega\varepsilon_0}\frac{\varepsilon_d}{\varepsilon_a\varepsilon_b}\begin{bmatrix} 0 & 0 & \cos\psi\sin\psi & -\cos^2\psi \\ 0 & 0 & \sin^2\psi & -\cos\psi\sin\psi \\ 0 & 0 & 0 & 0 \\ 0 & 0 & 0 & 0 \end{bmatrix}+$$
$$+\frac{\kappa^2}{\omega\varpi_0}\begin{bmatrix} 0 & 0 & 0 & 0 \\ 0 & 0 & 0 & 0 \\ -\cos\psi\sin\psi & \cos^2\psi & 0 & 0 \\ -\sin^2\psi & \cos\psi\sin\psi & 0 & 0 \end{bmatrix} \quad (42)$$

Given that the matrix $\left[\underline{\underline{P}}(k,\psi)\right]$ in the phononic medium is independent of Z, we have [25]:

$$\frac{d\left[f(L,\kappa,\psi,\omega)\right]}{\left[f(L,\kappa,\psi,\omega)\right]}=i\left[p(\kappa,\psi)\right]dz \quad (43)$$

After integration, we have:

$$\left[f(L,\kappa,\psi,\omega)\right]=\left[f(0,\kappa,\psi,\omega)\right]\exp\left\{i\left[p\right]L\right\} \quad (44)$$

Therefore, the transfer matrix of a thin columnar layer with thickness L will be as follows:

$$\left[M(L,\kappa,\psi,\omega)\right]=\exp\left[i\left[P(\kappa,\psi,\omega)\right]L\right] \quad (45)$$

2. Transfer matrix of the metal medium

Using the relations given in the previous section, the transfer matrix for a metal layer, which is a homogeneous layer, is as follows [25]:

$$\left[M(L_{met},\kappa,\psi,\omega)\right]=\exp\left[i\left[P_{met}(\kappa,\psi,\omega)\right]L_{met}\right] \quad (46)$$

where the kernel matrix will be as follows:

$$\left[P_{met}\right]=\begin{bmatrix} 0 & 0 & 0 & \mu_0 \\ 0 & 0 & -\mu_0 & 0 \\ 0 & -\varepsilon_0\varepsilon_{met} & 0 & 0 \\ \varepsilon_0\varepsilon_{met} & 0 & 0 & 0 \end{bmatrix}+$$
$$+\frac{\hat{\kappa}^2}{\omega\varepsilon_0\varepsilon_{met}}\begin{bmatrix} 0 & 0 & \sin\psi\cos\psi & -\cos^2\psi \\ 0 & 0 & \sin^2\psi & -\sin\psi\cos\psi \\ 0 & 0 & 0 & 0 \\ 0 & 0 & 0 & 0 \end{bmatrix}+$$
$$+\frac{\hat{\kappa}^2}{\omega\mu_0}\begin{bmatrix} 0 & 0 & 0 & 0 \\ 0 & 0 & 0 & 0 \\ -\sin\psi\cos\psi & \cos^2\psi & 0 & 0 \\ -\sin^2\psi & \sin\psi\cos\psi & 0 & 0 \end{bmatrix} \quad (47)$$

C. *Optical Absorption*

The Kretschmann configuration, as shown in Fig. 1, was utilized to facilitate the excitation and propagation of surface phonon-polariton (SPhP) waves at the metal–dielectric interface. Incident light with linear S- and P-polarizations illuminates the structure, from the homogeneous dielectric half-space (prism) at an angle θ relative to the z-axis and an azimuthal angle ψ relative to the x-axis in the xy plane.

The electromagnetic field of the incident plane wave in the region $z\le -L_{met}$ is expressed as follows [1]:

$$\mathbf{E}_{inc}(\mathbf{r})=\left(a_s\mathbf{s}+a_p\mathbf{P}_{inc}\right)\times$$
$$\times\exp\left[i\kappa\left(x\cos\psi+y\sin\psi\right)\right]\exp\left[ik_0n_sz\cos\theta_{inc}\right] \quad (48)$$

$$\mathbf{H}_{inc}(\mathbf{r}) = \frac{n_s}{\eta_0}(a_p\mathbf{s} + a_s\mathbf{P}_{inc}) \times \\ \times \exp\left[i\kappa\left(x\cos\psi + y\sin\psi\right)\right]\exp\left[ik_0 n_s z\cos\theta_{inc}\right] \quad (49)$$

where η_0 represents the intrinsic impedance, expressed in terms of the permeability of free space (μ_0) and the permittivity (ε_0) as follows:

$$\eta_0 = \sqrt{\frac{\mu_0}{\varepsilon_0}} \quad (50)$$

If n_s is the refractive index of the prism, $k = k_0 \sin\theta_{inc}$ represents the in-plane wave vector, where k_0 is the wave number in free space, and a_s and a_P are the amplitudes of the incident wave with S- and P-polarizations, respectively, the polarization unit vectors are defined in terms of Cartesian unit vectors as follows:

$$\mathbf{S} = -\hat{\mathbf{u}}_x \sin\psi + \hat{\mathbf{u}}_y \cos\psi \quad (51)$$

$$\mathbf{P}_{inc} = (-\hat{\mathbf{u}}_x \cos\psi + \hat{\mathbf{u}}_y \sin\psi)\cos\theta_{inc} + \hat{\mathbf{u}}_z \sin\theta_{inc} \quad (52)$$

The reflected components of the electromagnetic field, located in the half-space $z \le -L_{met}$, are expressed as follows:

$$\mathbf{E}_{ref}(\mathbf{r}) = (r_s\mathbf{s} + r_p\mathbf{P}_{ref}) \\ \exp\left[i\kappa\left(x\cos\psi + y\sin\psi\right)\right]\exp\left[-ik_0 n_s z\cos\theta_{ref}\right] \quad (53)$$

$$\mathbf{H}_{ref}(\mathbf{r}) = \frac{n_s}{\eta_0}(r_p\mathbf{s} + r_s\mathbf{P}_{ref}) \\ \exp\left[i\kappa\left(x\cos\psi + y\sin\psi\right)\right]\exp\left[-ik_0 n_s z\cos\theta_{inc}\right] \quad (54)$$

where:

$$\mathbf{P}_{ref} = (\hat{\mathbf{u}}_x \cos\psi + \hat{\mathbf{u}}_y \sin\psi)\cos\theta_{inc} + \hat{\mathbf{u}}_z \sin\theta_{inc} \quad (55)$$

where r_s and r_p are the amplitudes of the reflected light. For the transmitted components of the electromagnetic field located in the region $z \ge L_{ctf}$, we have:

$$\mathbf{E}_{tr}(\mathbf{r}) = (t_s\mathbf{s} + t_p\mathbf{P}_{tr})\exp\left[i\kappa\left(x\cos\psi + y\sin\psi\right)\right]\times \\ \times\exp\left[-ik_0 n_2 (z - L_S)\cos\theta_{tr}\right] \quad (56)$$

$$\mathbf{H}_{tr}(\mathbf{r}) = \frac{n_2}{\eta_0}(t_p\mathbf{s} + t_s\mathbf{P}_{tr})\exp\left[i\kappa\left(x\cos\psi + y\sin\psi\right)\right]\times \\ \times\exp\left[-ik_0 n_2 \left(z - L_\Sigma\right)\cos\theta_{tr}\right] \quad (57)$$

where:

$$\mathbf{P}_{tr} = (-\hat{\mathbf{u}}_x \cos\psi + \hat{\mathbf{u}}_y \sin\psi)\cos\theta_{tr} + \hat{\mathbf{u}}_z \sin\theta_{tr} \quad (58)$$

where t_s and t_p are the amplitudes of the transmitted light. In the given structure, n_2 represents the refractive index of vacuum, and equal to 1, and L_Σ denotes the total thickness of the layers. The angle of the transmitted light, θ_{tr} , can be determined using Snell's law in terms of the known incident angle:

$$n_1 \sin\theta_{inc} = n_2 \sin\theta_{tr} \quad (59)$$

$$\sin\theta_{tr} = \frac{n_1}{n_2}\sin\theta_{inc} \quad (60)$$

The amplitudes of the reflected and transmitted light can be determined using the continuity of the tangential components of the electric and magnetic fields, along with the transfer matrix method.

The relationship between the reflection and transmission coefficients and the amplitudes of the incident wave is given as follows:

$$\begin{bmatrix} r_s \\ r_p \end{bmatrix} = \begin{bmatrix} r_{ss} & r_{sp} \\ r_{ps} & r_{pp} \end{bmatrix}\begin{bmatrix} a_s \\ a_p \end{bmatrix} \quad (61)$$

$$\begin{bmatrix} t_s \\ t_p \end{bmatrix} = \begin{bmatrix} t_{ss} & t_{sp} \\ t_{ps} & t_{pp} \end{bmatrix}\begin{bmatrix} a_s \\ a_p \end{bmatrix} \quad (62)$$

In the above relations, identical indices indicate co-polarization, while different indices represent cross-polarization of the coefficients. The first index corresponds to the polarization type of the incident light, and the second index denotes the polarization type of the reflected or transmitted light. The reflectance and transmittance can then be calculated from the reflection and transmission coefficients as follows [43]:

$$\begin{cases} R_{ij} = \left| r_{ij} \right|^2 \\ T_{ij} = \dfrac{n_{air}}{n_{prism}} \dfrac{\mathrm{Re}\left\{ \cos\theta_{tr} \right\}}{\cos\theta_{in}} \left| t_{i,j} \right|^2 \end{cases} \rightarrow i, j = s, p \quad (63)$$

Finally, the optical absorption of the structure can be determined using the law of energy conservation for each polarization, based on the following relations [25,43]:

$$\begin{cases} A_s = 1 - \left(R_{ss} + R_{ps} + T_{ss} + T_{ps} \right) \\ A_p = 1 - \left(R_{pp} + R_{sp} + T_{pp} + T_{sp} \right) \end{cases} \quad (64)$$

IV. Results and Discussion

In this study, the propagation of surface phonon-polariton (SPhP) waves at the planar interface between a thin gold metal thin film and a columnar silicon carbide thin film was investigated using the Kretschmann configuration and the transfer matrix method.

To analyze the effect of each structural parameter on the excitation of surface phonon-polariton waves, reflectance intensity spectra for p-polarized incident light were plotted as a function of wavelength for varying structural and optical parameters. These spectra were obtained for porosity values (air volume fraction) ranging from 0.2 to 0.8, and the excitation of surface phonon-polaritons was thoroughly analyzed.

In this work, all resonance frequencies (ω) and linewidths are reported in energy units (eV) through the relation $E=\hbar\omega$. Therefore, whenever ω is expressed in eV, it denotes the corresponding energy $\hbar\omega$ rather than the angular frequency in rad/s.

A. *Air Volume Fraction*=0.2

In Fig. 4, the reflectance intensity spectra (R_p) as a function of the incident wavelength are presented for different growth angles of the silicon carbide nanocolumns at varying incident light angles. The structural parameters in these figures are d_{sic}=400 nm and d_{met}=30 nm. As shown in the Fig. 4, at x=15°, the dips shift slightly toward higher wavelengths as the incident light angle increases. The longitudinal and transverse optical frequencies are approximately in the ranges ω_{L0}=0.098eV and ω_{T0}=0.097eV, respectively. This region is referred to as the "Reststrahlen band" where optical phonons couple with polarized photons, resulting in a minimum in the reflection spectrum and a corresponding peak in the absorption spectrum. Additionally, it is evident that the reflection dip deepens with increasing incident light angle, leading to a stronger coupling between surface phonons and polarized photons. At x=30, similar behavior is observed, with the dips becoming slightly deeper and the longitudinal and transverse optical frequencies shifting to approximately ω_{L0} =0.097eV and ω_{T0}=0.096 eV, respectively. The Reststrahlen bandwidth slightly increases. At x=45°, for incident light angles of θ=15° and θ=30°, no deep dips are observed. At θ=45°, the transverse optical frequency is ω_{T0}=0.0953eV and the longitudinal optical frequency is ω_{L0}=0.0958 eV, with a Reststrahlen bandwidth of 0.0015 eV. At θ=50°, the transverse optical frequency is ω_{T0}=0.0951eV, the longitudinal optical frequency is ω_{L0}=0.0968eV, and the Reststrahlen bandwidth is 0.0017 eV. At θ=75°, the transverse optical frequency is ω_{T0}=0.0950eV, the longitudinal optical frequency is ω_{L0}=0.0968eV, and the Reststrahlen bandwidth is 0.0018 eV. At x=60°, no deep dips were observed at incident light angles θ=15° and θ=30°, which would allow for the extraction of the Reststrahlen band. At θ=45°, the transverse optical frequency is ω_{T0}=0.0943eV and the longitudinal optical frequency is ω_{L0}=0.0958eV, with a Reststrahlen bandwidth of 0.0015 eV. At θ=50°, the transverse optical frequency is ω_{T0}=0.0951 eV, the longitudinal optical frequency is ω_{L0}=0.0968eV, and the

Reststrahlen bandwidth is 0.0017 eV. At θ=75°, the transverse optical frequency is ω_{T0}=0.0950 eV, the longitudinal optical frequency is ω_{L0}=0.0968 eV, and the Reststrahlen bandwidth is 0.0018 eV. At higher incident light angles, the reflection dips, indicating greater absorption, become deeper. However, no significant changes in the reflection dips were observed at incident light angles of θ=15° and θ=30°. Therefore, the Reststrahlen band is not clearly visible in these regions, and the measurement of the Reststrahlen bandwidth was carried out for incident light angles from θ=45° to θ=75°. In this range, as the growth angle of the nanocolumns (x) increases, the Reststrahlen bandwidth also increases.

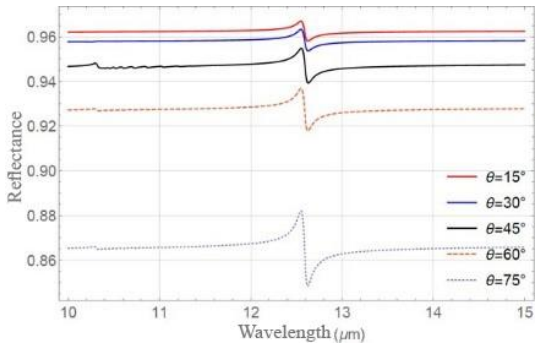

(a)

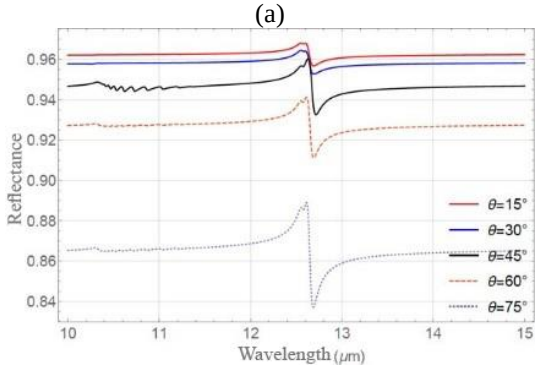

(b)

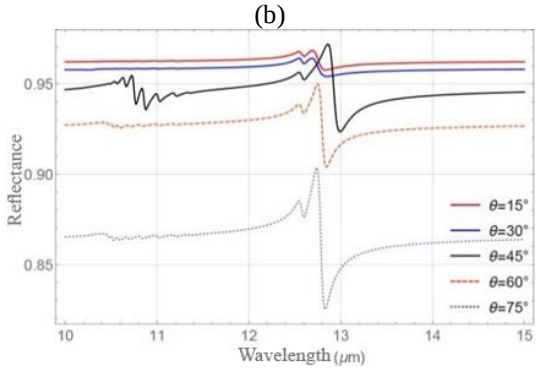

(c)

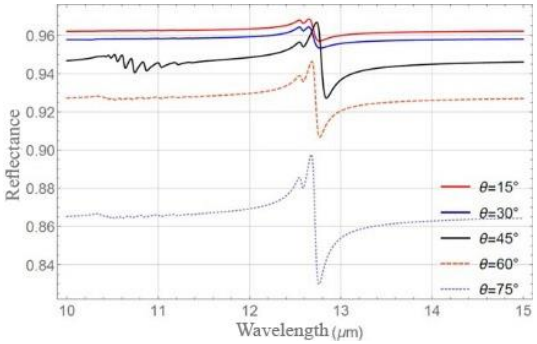

(d)

Fig. 4. Reflectance spectra of the metal-columnar thin-film structure with a porosity of 0.2 for values of (a) x=15°, (b) x=30°, (c) x=45°, and (d) x=60°.

In Fig. 5, the reflectance spectra R_p as a function of the incident wavelength are plotted for various thicknesses of the metallic thin layer at different growth angles of silicon carbide nanocolumns. The fixed structural parameters in this figure are d_{SiC}=200 nm and x=15°. When the metallic layer thickness d_{met} is zero, meaning that only the silicon carbide columnar thin film is present, two reflection peaks appear at a wavelength of λ=12.5 μm for low incident angles (θ=15° and θ=30°). At higher incident angles (θ=45°, 60°, and 75°), deep valleys are evident in the reflectance spectra. These peaks and valleys are compensated in the transmission spectra (not shown here), indicating that coupling between polarized photons and optical phonons does not occur. For d_{met}=10 nm, at an incident angle of θ=15°, the transverse optical frequency is ω_{T0}=0.0977eV, the longitudinal optical frequency is ω_{L0}=0.0984eV, and the Reststrahlen bandwidth is 0.0007eV.

For θ=30°, ω_{T0}=0.0986 eV ω_{L0}=0.0985eV, and the bandwidth is 0.0009eV. At θ=45°, ω_{T0}=0.0974 eV, ω_{L0}=0.0976eV, and the bandwidth is 0.0012eV. At θ=50°, ω_{T0}=0.0970eV, ω_{L0}=0.0985eV, and the bandwidth is 0.0015eV. Finally, at θ=75°, ω_{T0}=0.0971eV, ω_{L0}=0.0986eV, and the bandwidth is 0.0018eV. The strongest excitation of surface polariton-phonon waves occurs at d_{met}=10 nm, with the Reststrahlen bandwidth increasing with the incident angle, reaching a maximum value of 0.0018eV. As the metallic layer thickness increases beyond 10 nm, the reflectance intensity decreases because the incident light penetrates the

metallic layer, reducing the opportunity for surface polariton-phonon wave excitation at the metal-dielectric interface. For d_{met}=20 nm, the Reststrahlen band is not significant at incident angles of 15° and 30°. At θ=45°, ω_{T0}=0.0976eV, ω_{L0}=0.0985eV, and the bandwidth is 0.0096eV. For θ=50°, ω_{T0}=0.0974eV, ω_{L0}=0.0986eV, and the bandwidth is 0.0012eV. At θ=75°, ω_{T0}=0.0974eV, ω_{L0}=0.0986eV, and the bandwidth remains 0.0012eV. For d_{met}=30 nm, at the highest incident angle (θ=75°), a noticeable Reststrahlen band is observed with ω_{T0}=0.0976eV, ω_{L0}=0.0985eV, and a bandwidth of 0.0096eV.

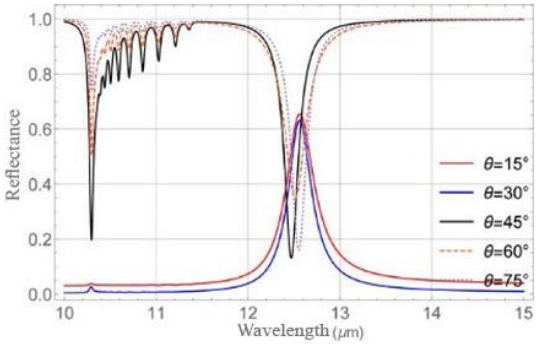

(a)

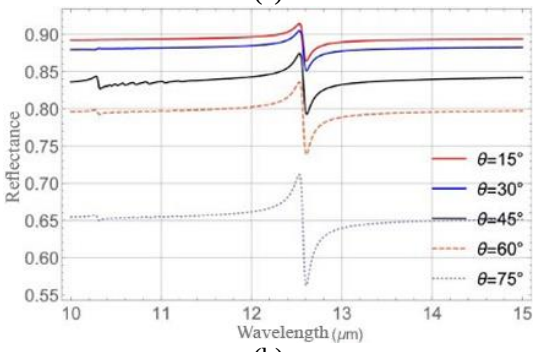

(b)

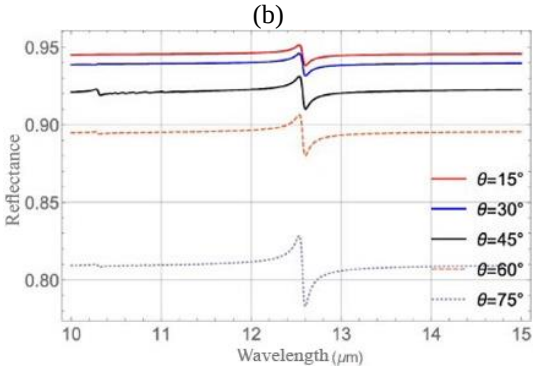

(c)

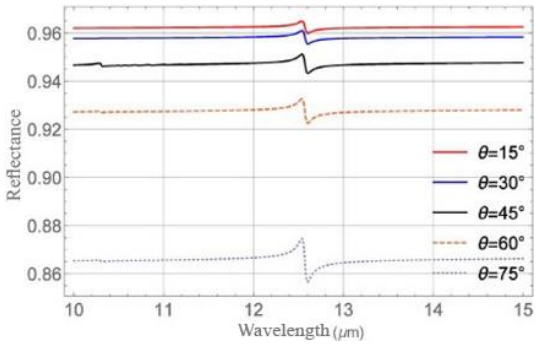

(d)

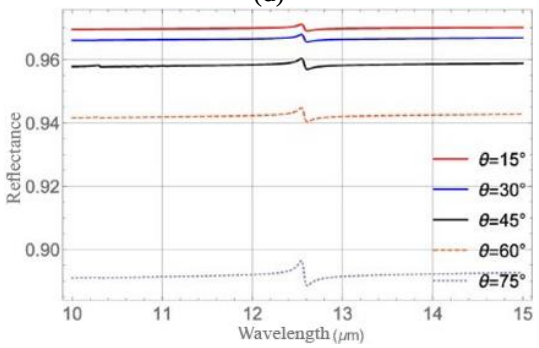

(e)

Fig. 5. Reflectance spectra of the metal-columnar thin film structure with a porosity of 0.2 and thickness of the metal thin film of (a) d_{met}=0 nm, (b) d_{met}=10 nm, (c) d_{met}=20 nm, (d) d_{met}=30 nm, and (e) d_{met}=40 nm.

In Fig. 6, the effect of the thickness of silicon carbide nanocolumns is analyzed for fixed parameters d_{met}=30 nm and x=15°. Within this range, increasing the thickness of the nanocolumns results in a noticeable increase in the depth of the reflectance minima. It is evident that in the absence of silicon carbide, the spectra are completely flat and featureless. At a thickness of 100 nm, no Reststrahlen band is observed at low incident angles (θ=15° and θ=30°), and the reflectance spectra remain smooth and without any minima. As the angle of incidence increases, the minima become apparent. At d_{SiC}=200 nm and θ=75°, the transverse optical frequency is ω_{T0}=0.0977eV, the longitudinal optical frequency is ω_{L0}=0.0980eV, and the bandwidth is 0.003eV. At θ=50°, ω_{T0} =0.0979eV, ω_{L0}=0.0985eV. At θ=45°, ω_{T0}=0.0980eV, ω_{L0}=0.0985eV. At d_{SiC}=300 nm and θ=75°, ω_{T0}=0.0974eV, ω_{L0}=0.0985eV, with a bandwidth of 0.011eV. At θ=50°, ω_{T0}=0.0977eV, ω_{L0}=0.0984eV. At θ=45°, ω_{T0} =0.0977eV, ω_{L0}=0.0984eV. At d_{SiC}=400 nm and θ=75°, ω_{T0}=0.0971eV, ω_{L0}=0.0984eV, with a bandwidth of 0.013eV.

At θ=50°, ω_{T0}=0.0974eV, ω_{L0}=0.0984eV. At θ=45°, ω_{T0}=0.0975eV, ω_{L0}=0.0983eV. At d_{SiC}=500 nm and θ=75°, ω_{T0}=0.0967eV, ω_{L0}=0.0984eV, with a bandwidth of 0.0017eV. At θ=50°, ω_{T0}=0.0973eV, ω_{L0}=0.0982eV, with a bandwidth of 0.0009eV. At θ=45°, ω_{T0}=0.0974eV, ω_{L0}=0.0983eV. As the thickness of silicon carbide nanocolumns increases, the depth of the reflectance minima relatively increases, and the Reststrahlen band bandwidth becomes wider. The maximum Reststrahlen bandwidth of 0.0018eV is observed at d_{SiC}=600 nm and an incident angle of θ=75°.

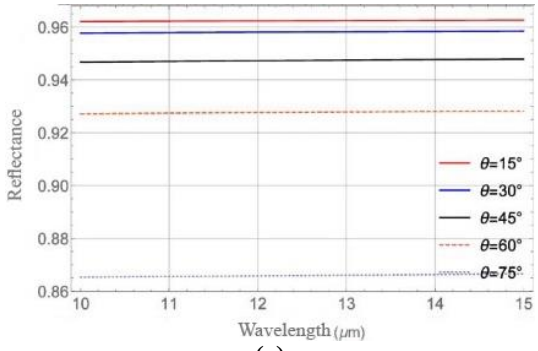

(a)

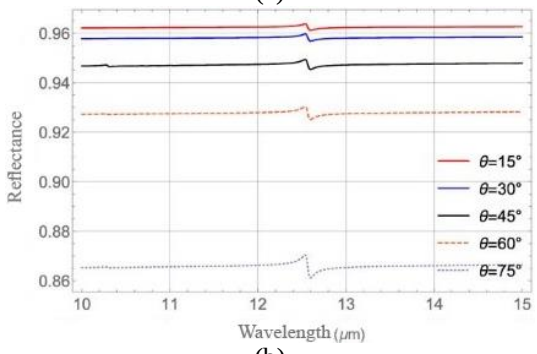

(b)

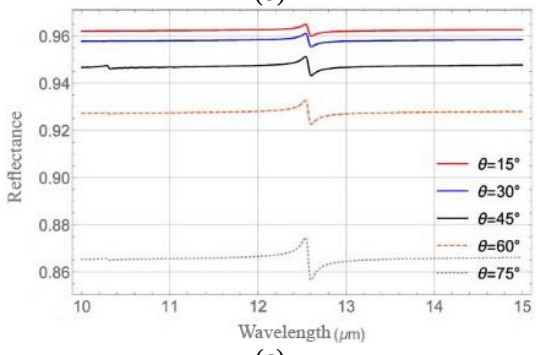

(c)

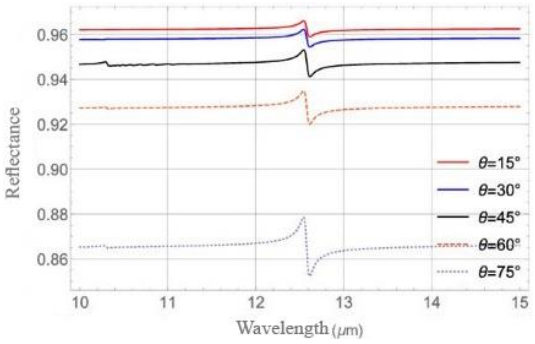

(d)

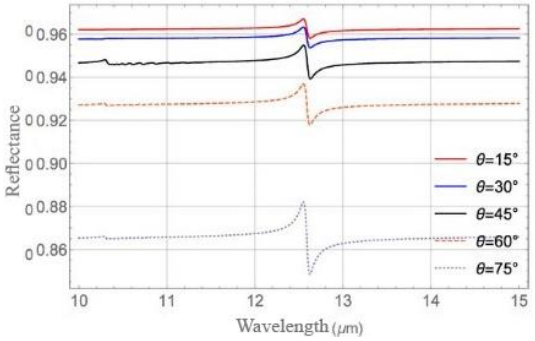

(e)

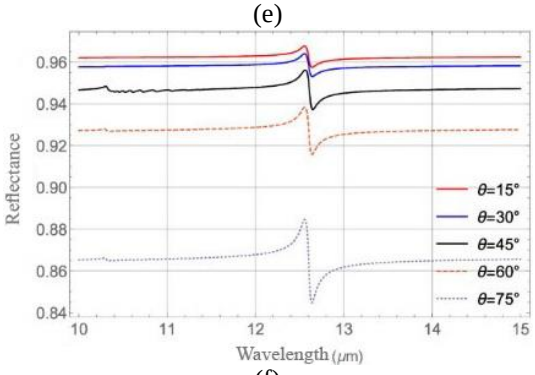

(f)

Fig. 6. Reflectance spectra of the metal-columnar thin film structure with a porosity of 0.2 and thickness of columnar silicon carbide thin film of (a) d_{sic}=0 nm, (b) d_{sic}=100 nm, (c) d_{sic}=200 nm, (d) d_{sic}=300 nm, (e) d_{sic}=400 nm, and (f) d_{sic}=500 nm.

B. *Air Volume Fraction*=0.4

The effect of porosity up to 0.4 in silicon carbide and its impact on surface phonon-polariton excitation under different structural and optical parameters were investigated.in Fig. 7. Initially, the variation of the growth angle of nanocolumns for fixed values of d_{met}=30 nm and d_{SiC}=400 is shown in Fig. 6. At incident light angles of θ=15° and θ=30°, no significant surface phonon-polariton excitation was observed for any nanocolumn growth angle. At x=15°, with an incident light angle of θ=45°, the transverse optical frequency ω_{T0}=0.0978eV, longitudinal optical frequency ω_{L0}=0.0985eV, and the Reststrahlen bandwidth

(f)

0.0008eV were observed. At θ=50°, ω_{T0}=0.0977eV, ω_{L0}=0.0985eV, and the Reststrahlen bandwidth remained 0.0008eV. At θ=75°, ω_{T0}=0.0974eV, ω_{L0}=0.0984eV, and the bandwidth increased to 0.0010eV. For x=30°, at θ=45°, the transverse optical frequency ω_{T0}=0.0974eV, longitudinal optical frequency ω_{L0}=0.0981eV, and the bandwidth 0.0007eV. At θ=50°, ω_{T0}=0.0974eV, ω_{L0}=0.0983eV, and the bandwidth 0.0009eV. At θ=75°, ω_{T0}=0.0967eV, ω_{L0}=0.0982eV, and the bandwidth 0.0015eV. For x=45°, at θ=45°, the transverse optical frequency ω_{T0}=0.0967eV, longitudinal optical frequency ω_{L0}=0.0977eV, and the bandwidth 0.0010eV. At θ=50°, ω_{T0}=0.0966eV, ω_{L0}=0.0980eV, and the bandwidth 0.0011eV. At θ=75°, ω_{T0}=0.0965eV, ω_{L0}=0.0981eV, and the bandwidth 0.0016eV. For x=60°, at θ=45°, the transverse optical frequency ω_{T0}=0.0963eV, longitudinal optical frequency ω_{L0}=0.0974eV, and the bandwidth 0.0011eV. At θ=50°, ω_{T0}=0.0968eV, ω_{L0}=0.0979eV, and the bandwidth 0.0011eV. At θ=75°, ω_{T0}=0.0966eV, ω_{L0}=0.0979eV, and the bandwidth 0.0013eV. From θ=45° to θ=75°, with increasing growth angles of nanocolumns, the reflectivity intensity increased. The Reststrahlen bandwidth at θ=75° and x=60° reached its maximum value of 0.0013eV.

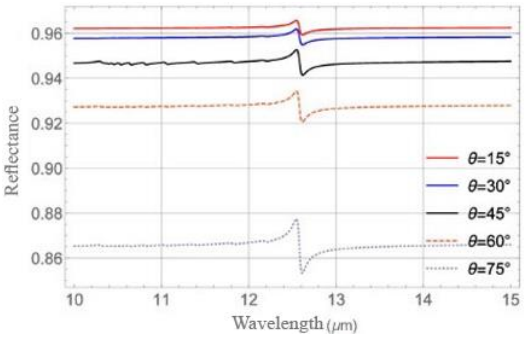

(a)

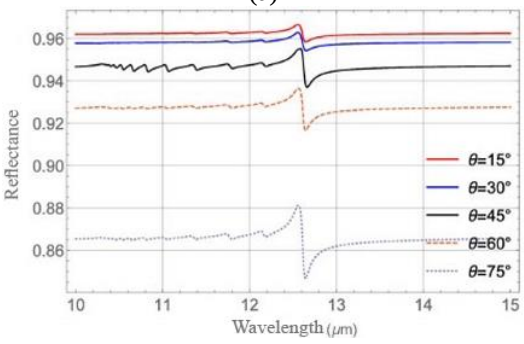

(b)

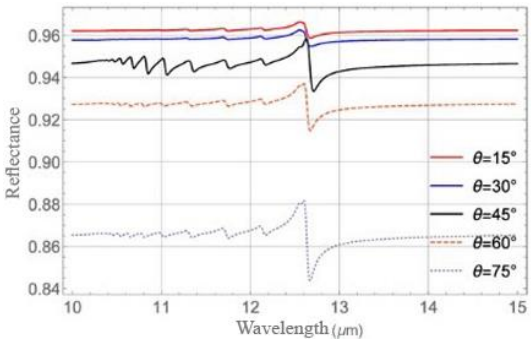

(c)

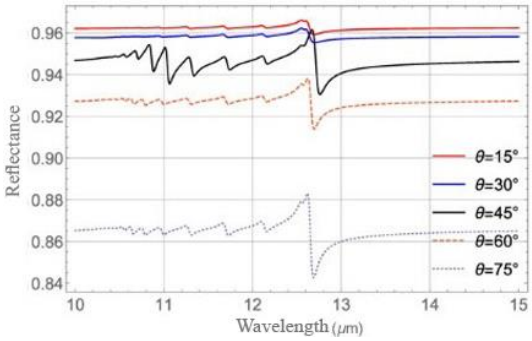

(d)

Fig. 7. Reflectance spectra of the metal-columnar thin-film structure with a porosity of 0.4 for values of (a) x=15°, (b) x=30°, (c) x=45°, and (d) x=60°.

Figure. 8 shows the effect of metal layer thickness on SiC porosity of 0.4 for fixed parameters (d_{SiC}=200 nm, vapor angle x=15°). When the metal layer thickness was zero, the reflection spectra at incident light angles of θ=15° and θ=30° only showed intensity peaks, whereas at θ=45°, θ=50°, and θ=75°, valleys were observed, compensating for these peaks in transmission spectra. At d_{met}=10 nm and θ=15°, ω_{T0}=0.0978eV, ω_{L0}=0.0986eV, and bandwidth 0.0008eV. For θ=30°, ω_{T0}.0977eV, ω_{L0}=0.0986eV, and bandwidth 0.0009eV. For θ=45°, ω_{T0}=0.0976eV, ω_{L0}=0.0986eV, and bandwidth 0 0.0010eV. Similarly, at θ=50°, ω_{T0}=0.0976eV, ω_{L0}=0.0986eV, and bandwidth 0.0010eV. At θ=75°, ω_{T0}=0.0974eV, ω_{L0}=0.0986eV, and bandwidth 0.0012eV. Increasing the metal layer thickness flattened the reflection spectra, and no Reststrahlen band was observed.

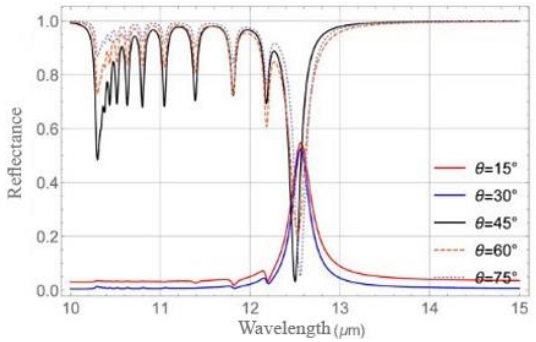

(a)

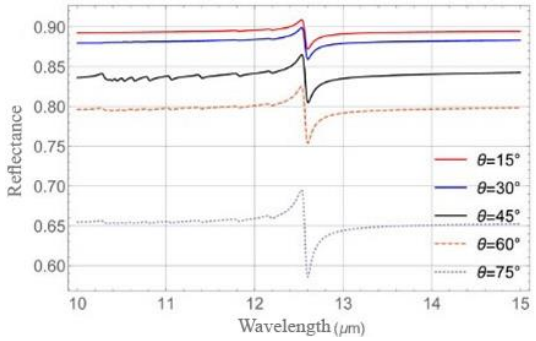

(b)

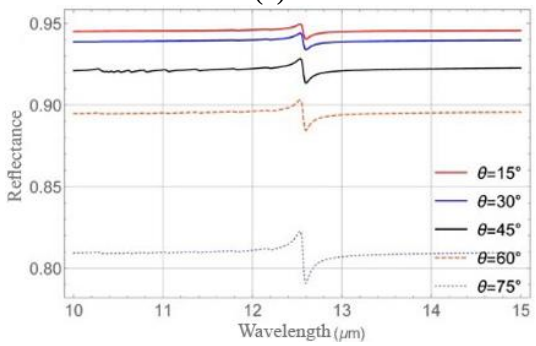

(c)

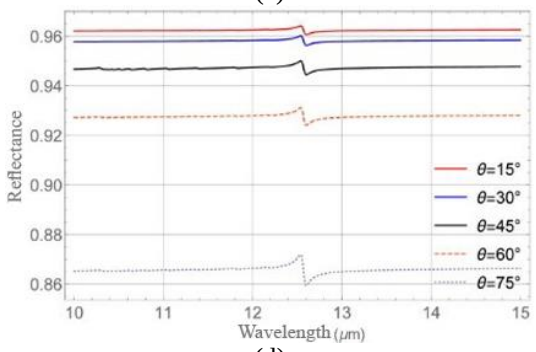

(d)

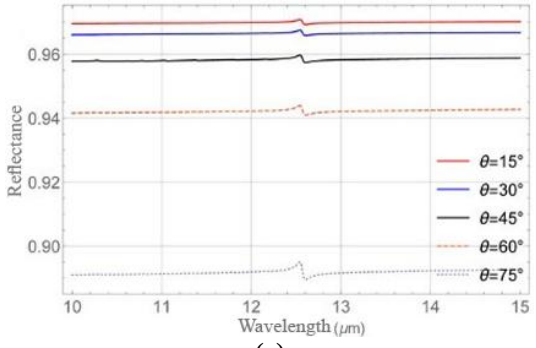

(e)

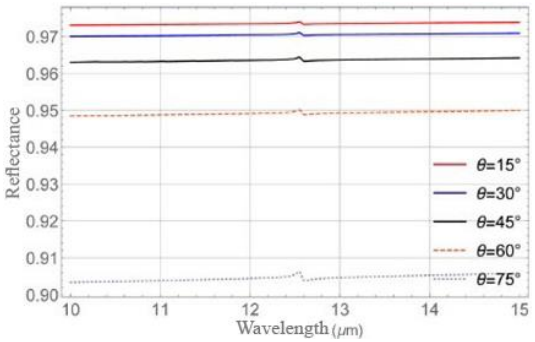

(f)

Fig. 8. Reflectance spectra of the metal-columnar thin film structure with a porosity of 0.4 and thickness of the metal thin film of (a) d_{met}=0 nm, (b) d_{met}=10 nm, (c) d_{met}=20 nm, (d) d_{met}=30 nm, (e) d_{met}=40 nm, and (f) d_{met}=50 nm.

In Fig. 9, the effect of SiC nanocolumn thickness at a porosity of 0.4, fixed parameters (d_{met}=30nm, x=15°), is analyzed. As the SiC nanocolumn thickness increases, the depth of valleys in the reflection spectra rises under higher incident angles. In Figs. 9(a–c), no Reststrahlen band was observed. At d_{SiC}=300nm, the deepest valley at θ=75° corresponds to ω_{T0}=0.0977eV, ω_{L0}=0.0987eV, and bandwidth 0.0010eV. At d_{SiC}=400 nm, the deepest valley at θ=75° corresponds to ω_T=0.0974eV, ω_L=0.0986eV, and bandwidth 0.0012eV. At d_{SiC}=500 nm, the deepest valley at θ=75° corresponds to ω_{T0}=0.0972eV, ω_{L0}=0.0985eV, and bandwidth 0.0013eV. Generally, in Fig. 9, at incident light angles of θ=15° and θ=30°, no reflective valleys are observed. However, as the thickness of nanocolumns increases, the Reststrahlen bandwidth rises for incident light angles of θ=45°, θ=50°, and θ=75°.

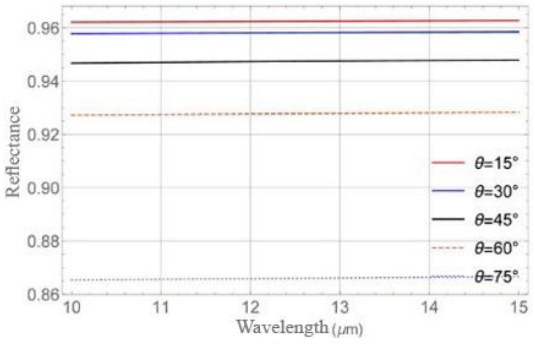

(a)

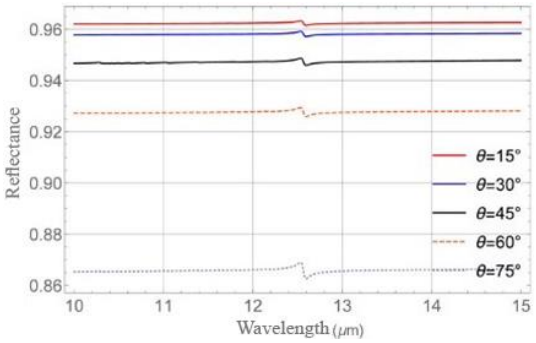

(b)

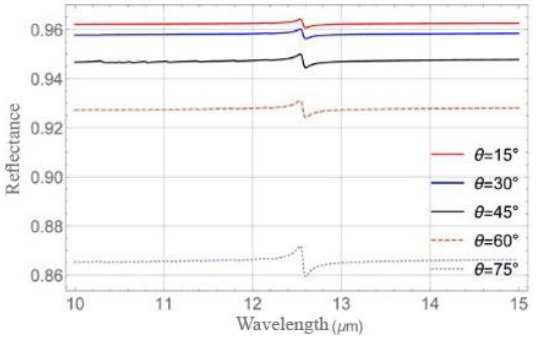

(c)

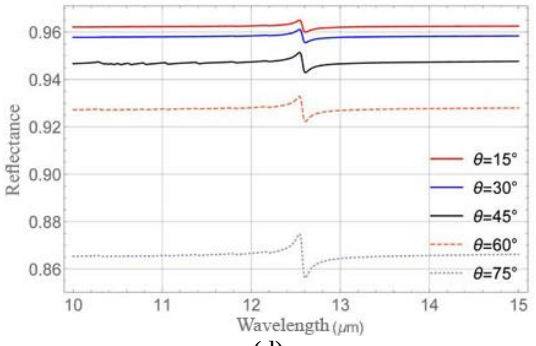

(d)

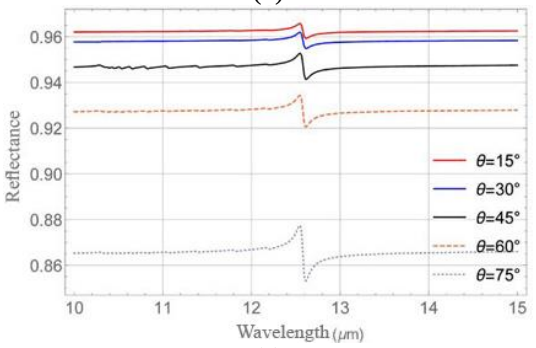

(e)

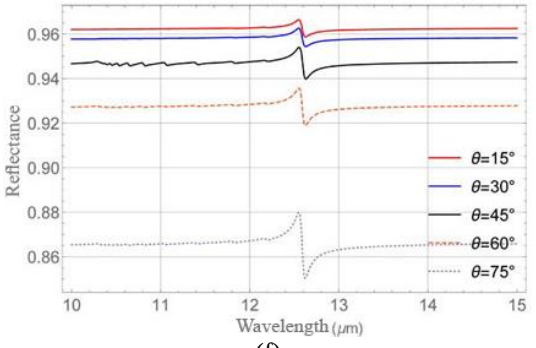

(f)

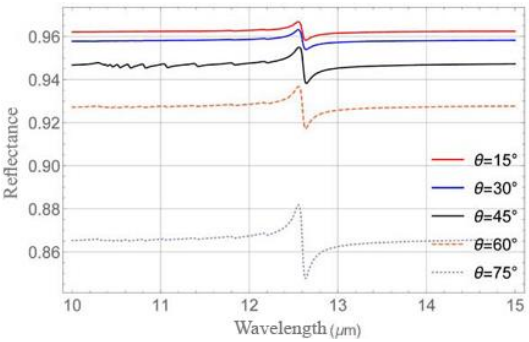

(g)

Fig. 9. Reflectance spectra of the metal-columnar thin film structure with a porosity of 0.4 and thickness of columnar silicon carbide thin film of (a) d_{sic}=0 nm, (b) d_{sic}=100 nm, (c) d_{sic}=200 nm, (d) d_{sic}=300 nm, (e) d_{sic}=400 nm, (f) d_{sic}=500 nm, and (g) d_{sic}=600 nm.

C. *Air Volume Fraction*=0.6

In Fig. 10, the effect of the growth angle of nanocolumns, x, at a porosity of 0.6 is shown for fixed parameters d_{SiC}=400 nm and d_{met}=30 nm. At growth angles x=15° and x=30°, no reflection dips are observed. However, at angles x=45 to x=60°, peaks and dips appear in the reflection spectrum, which cannot be attributed to surface phonon-polariton excitation.

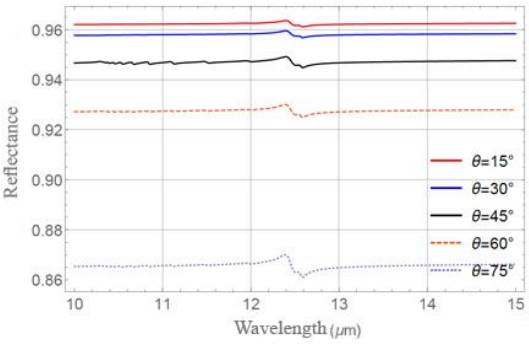

(a)

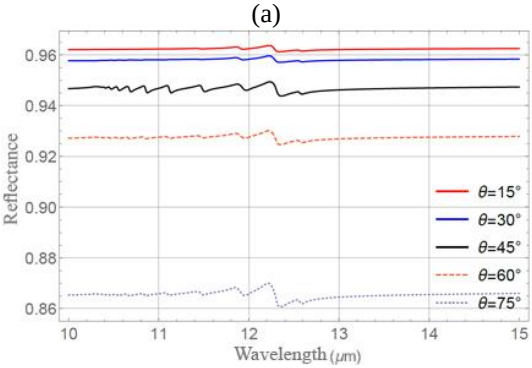

(b)

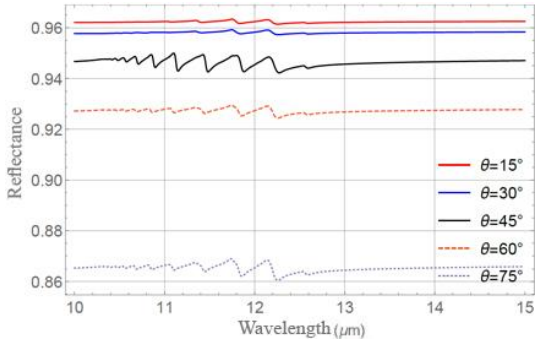

(c)

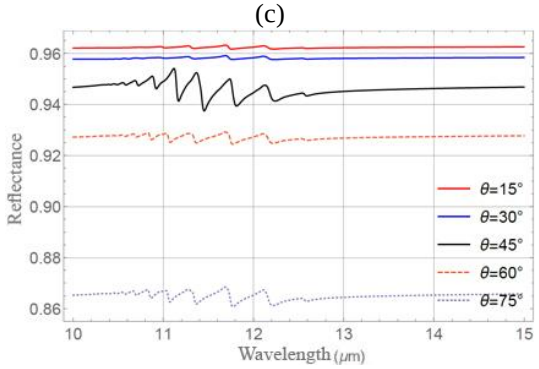

(d)

Fig. 10. Reflectance spectra of the metal-columnar thin-film structure with a porosity of 0.6 for values of (a) x=15°, (b) x=30°, (c) x=45°, and (d) x=60°.

In Fig. 11, the influence of the metal thin film thickness on surface phonon-polariton excitation is depicted for fixed parameters d_{SiC}=200nm and x=15°. Except for a metal layer thickness of d_{met}=10 nm, no reflection dips indicative of surface phonon-polariton excitation are observed in the spectra. When the metal layer thickness is d_{met}=10 nm, the Reststrahlen bandwidth is 0.0023eV, and increasing the incident light angle does not affect this value. At incident light angles of θ=15° and θ=30°, no Reststrahlen bands are formed in any of the spectra.

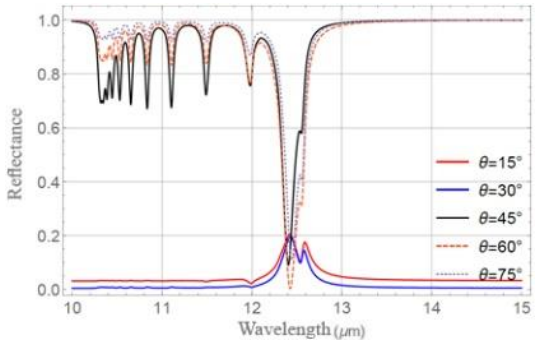

(a)

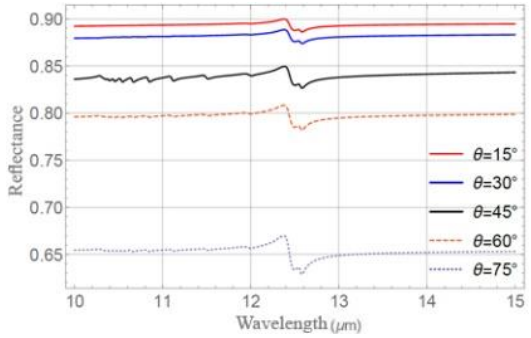

(b)

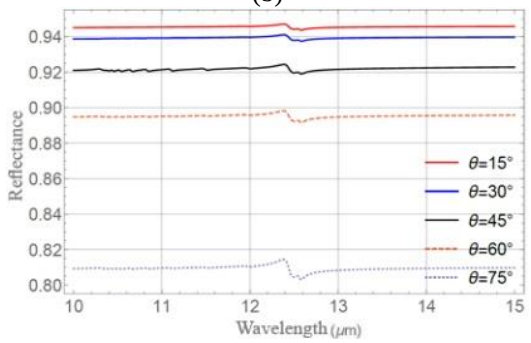

(c)

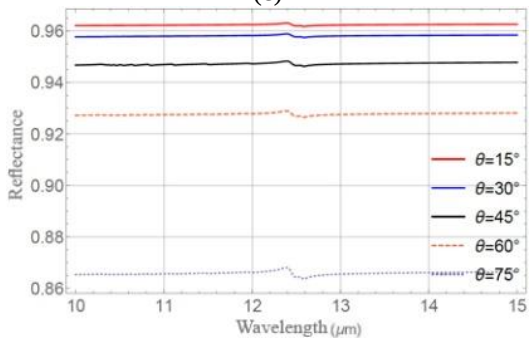

(d)

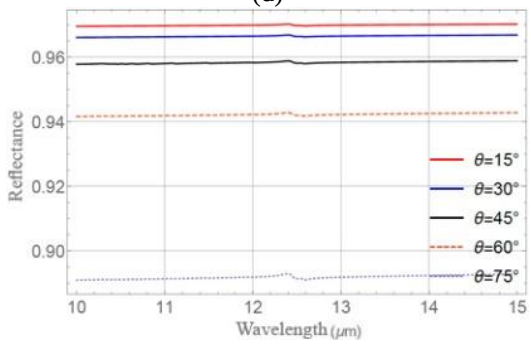

(e)

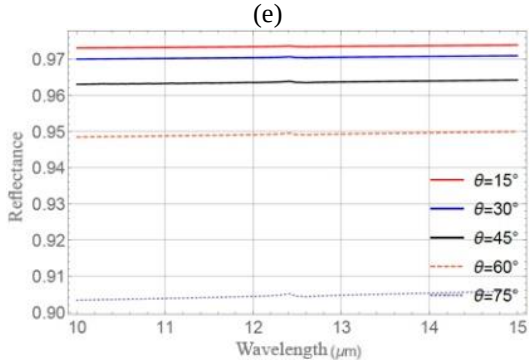

(f)

Fig. 11. Reflectance spectra of the metal-columnar thin film structure with a porosity of 0.6 and

thickness of the metal thin film of (a) dmet=0 nm, (b) d_{met}=10 nm, (c) d_{met}=20 nm, (d) d_{met}=30 nm, (e) d_{met}=40 nm, and (f) d_{met}=50 nm.

In Fig. 12, the effect of the thickness of silicon carbide nanocolumns on surface phonon-polariton excitation is presented for fixed parameters d_{met}=30 nm and x=15°. At a porosity of 0.6, prominent reflection dips occur at thicknesses d_{SiC}=400 nm, d_{SiC}=500 nm, and d_{SiC}=600 nm at a wavelength of 12.4 μm and incident light angles θ=45°, θ=50°, and θ=75°. At incident light angles θ=15° and θ=30°, the spectra exhibit no dips. The depth of the dips is insufficient to calculate the Reststrahlen bandwidth. Thus, it can be concluded that at this level of porosity, changes in the thickness of the nanocolumns have no significant effect on the Reststrahlen bandwidth.

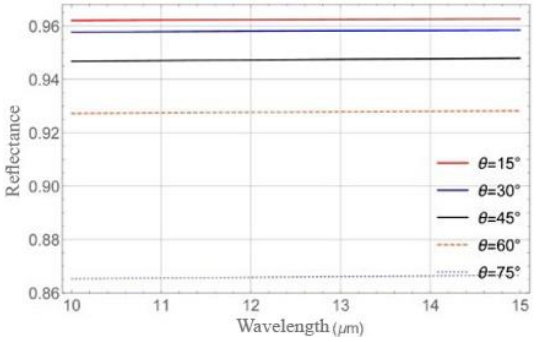

(a)

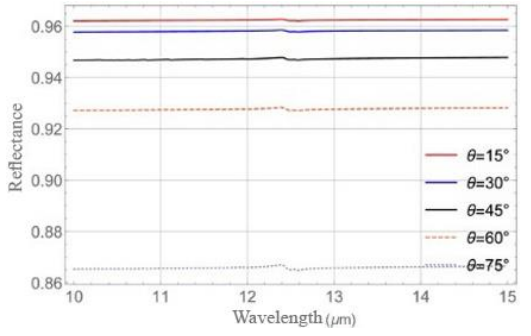

(b)

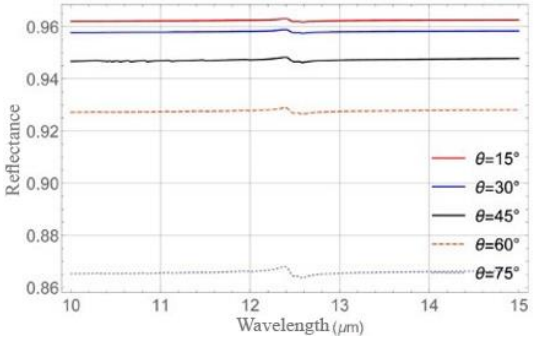

(c)

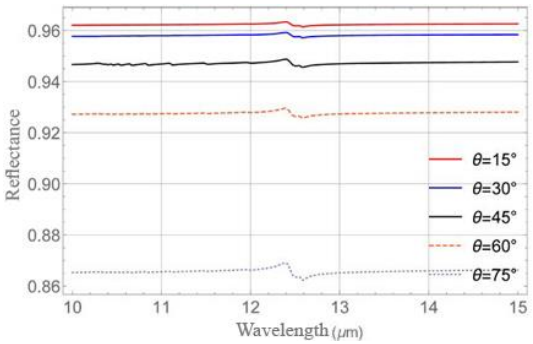

(d)

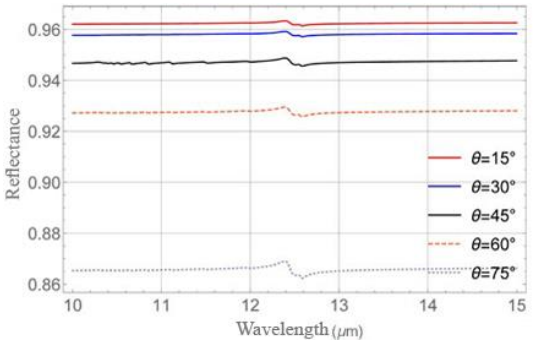

(e)

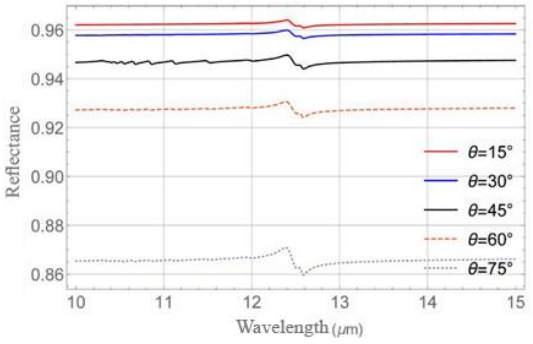

(f)

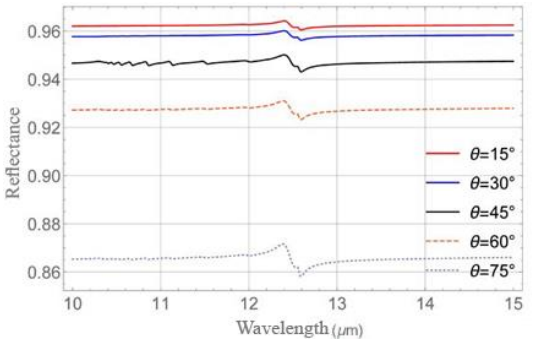

(g)

Fig. 12. Reflectance spectra of the metal-columnar thin film structure with a porosity of 0.6 and thickness of columnar silicon carbide thin film of (a) *dsic*=0 nm, (b) *dsic*=100 nm, (c) *dsic*=200 nm, (d) *dsic*=300 nm, (e) *dsic*=400 nm, (f) *dsic*=500 nm, (g) *dsic*=600 nm.

D. *Air Volume Fraction*=0.8

In Fig. 13, the effect of the growth angles of silicon carbide nanocolumns at a porosity of 0.8 is illustrated. At a growth angle of x=45°, the

reflection intensity at an incident light angle of θ=45° reaches its maximum value. The transverse optical frequency (ω_{T0}) is 0.1038 eV, the longitudinal optical frequency (ω_{L0}) is 0.1050 eV, and the Reststrahlen bandwidth in this range is 0.0012 eV. At vapor deposition angles of x=15° and x=30°, no reflection dips are observed, and no Reststrahlen band is formed.

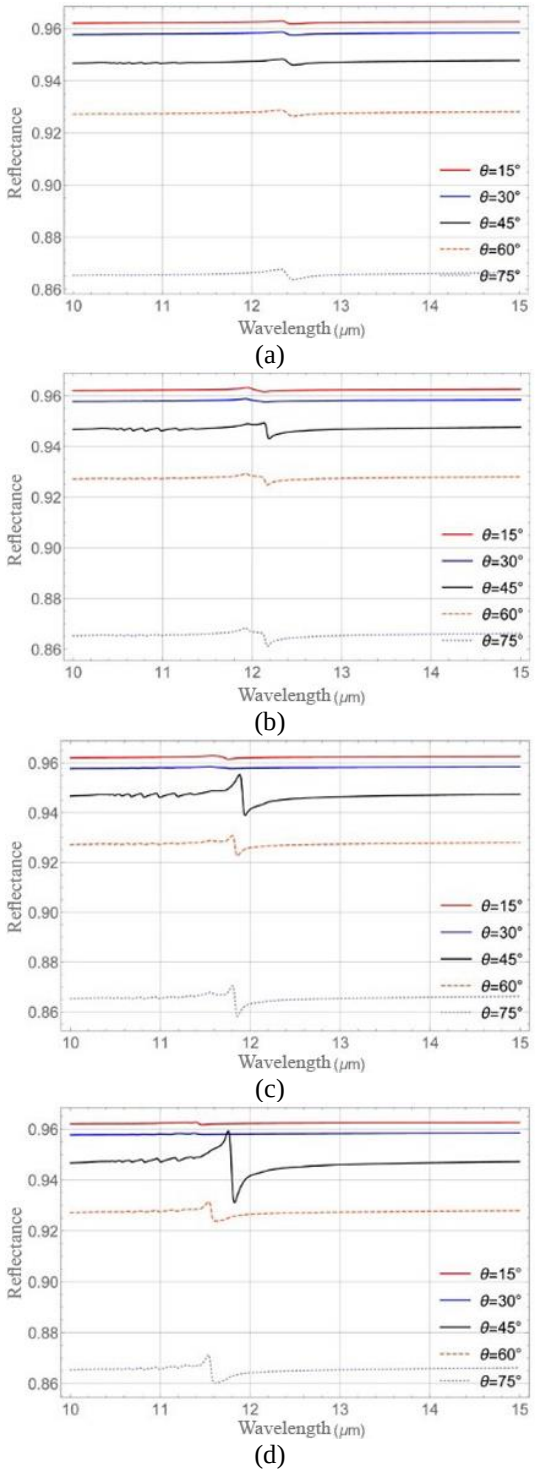

Fig. 13. Reflectance spectra of the metal-columnar thin-film structure with a porosity of 0.8 for values of (a) x=15°, (b) x=30°, (c) x=45°, and (d) x=60°.

In Fig. 14, the effect of the metal thin film thickness on reflection spectra at a porosity of 0.8 is presented. Due to the low density of the columnar silicon carbide thin film in this porosity, surface phonon-polariton excitation in the reflection spectra is very weak. For a metal layer thickness of d_{met}=10nm, reflection dips are observed at higher incident light angles in the wavelength range of 12.42 μm. However, this range is not regarded as a Reststrahlen band.

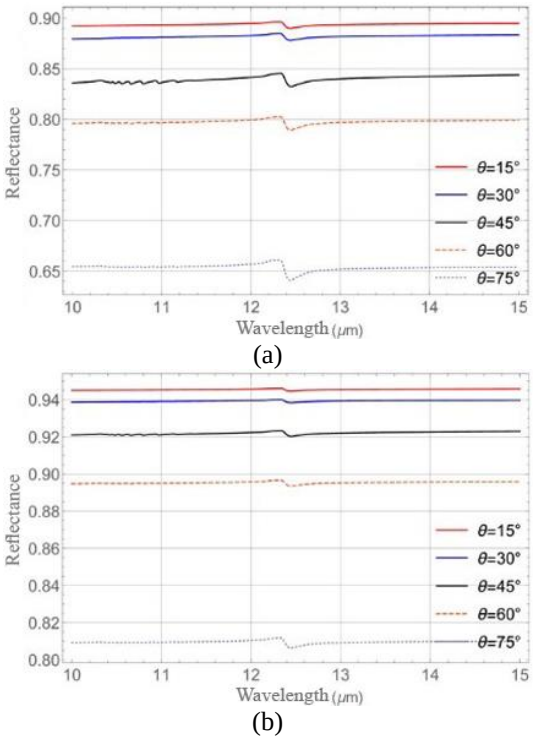

Fig. 14. Reflectance spectra of the metal-columnar thin film structure with a porosity of 0.8 and thickness of the metal thin film of (a) d_{met}=10 nm, (b) d_{met}=20 nm.

the effect of the thickness of silicon carbide nanocolumns on surface phonon-polariton excitation at a porosity of 0.8 is depicted. At this high porosity and extremely low silicon carbide density, no excitation occurs, and the reflection spectrum remains entirely smooth. Thus, variations in the thickness of silicon carbide nanocolumns do not affect the reflection spectra.

V. The Comparison of the Results of Different Porosity Fractions

Based on the reflectance spectra of the proposed structure, plotted as a function of wavelength for various values of x and fixed parameters of d_{met}=30 nm and d_{sic}=400 nm, the strongest excitation occurs at the vapor angle x_v=45° and x_v=60° for a porosity of f_v=0.2, with the maximum reflectance dip observed at an incidence angle θ=75°. The deepest reflectance dip is observed at x_v=60°, f_v=0.2, and a wavelength of 12.83μm. This dip becomes shallower for the same x_v=60° and θ=75° when the porosity increases to f_v=0.4. The highest frequency of the Reststrahlen band occurs at f_v=0.2, x_v=45°, and θ=75°, with a value of 0.0023eV. As the porosity increases to f_v=0.4, this frequency decreases to 0.0016eV. The trend of decreasing intensity of surface phonon-polariton (SPhP) excitation becomes more pronounced for f_v=0.6 and f_v=0.8. At f_v=0.6, SPhP excitations are no longer observed for changes in x, and the Reststrahlen band disappears entirely. From the reflectance spectra at f_v=0.8, it is evident that SPhP excitations are generally absent, except at x_v=60°. Even then, at θ=45° and x_v=60°, the Reststrahlen bandwidth is 0.0012eV, which previously appeared at θ=75° for f_v=0.2 and f_v=0.4. Upon increasing the porosity to f_v=0.8, the position shifts to θ=45°. For comparing the effect of porosity on SPhP excitation within the reflectance spectra of the structure, variations in the thickness of the gold layer reveal that at d_{met}=10 nm, the strongest excitation occurs at f_v=0.2. The deepest reflectance dip is found at θ=75° and a wavelength λ=12.52 μm. The frequency of the Reststrahlen band reaches its maximum value of 0.0019eV in this region. Increasing the porosity to f_v=0.4 reduces both the excitation intensity and bandwidth, which decreases to 0.0012eV. This reduction in the intensity and width of the Reststrahlen band becomes significant as the porosity increases, such that at f_v=0.8, SPhP excitation nearly vanishes. Examining the reflectance spectra as a function of wavelength and variations in the silicon carbide nanocolumn thickness reveals that the maximum excitation intensity occurs at θ=75° and d_{sic}=600 nm. The deepest reflectance dip, observed at f_v=0.2, λ=12.652μm, and R_P=0.84, decreases with increasing porosity. The Reststrahlen band reaches its maximum bandwidth of 0.0018eV at f_v=0.2 and d_{sic}=600 nm. With increasing porosity, this value decreases, dropping to 0.0014eV at f_v=0.4. For f_v=0.6 and f_v=0.8, no Reststrahlen band formation is observed.

VI. Surface Phonon-Polariton Excitation at the Presence of a Homogeneous and Isotropic Silicon Carbide Dielectric Layer

In Fig. 15, the excitation of surface phonon-polariton waves at the interface of a thin gold layer and a homogeneous, isotropic silicon carbide (SiC) layer was analyzed for d_{met}=30nm. As observed in the figure, increasing the thickness of the homogeneous dielectric layer leads to deeper dips in the reflectance spectrum, with the deepest dip occurring at d_{SiC}=300 nm, an incident angle of θ=75°, and λ=12.88 μm. The maximum Reststrahlen bandwidth is 0.0026eV, which is found in the same region. At the same thickness, d_{SiC}=300nm, reducing the incident light angle diminishes the Reststrahlen bandwidth and the depth of the reflectance dips, to the extent that at θ=15° and θ=30°, no noticeable reflection dip or Reststrahlen band exists. Compared to the columnar thin-film structure of silicon carbide, the Reststrahlen band in the homogeneous layer is stronger. At θ=45°, a shallower dip is observed in the reflectance spectrum of the metal-homogeneous dielectric structure, which was not present in the spectrum of the metal-inhomogeneous dielectric structure. Reducing the thickness of the homogeneous dielectric layer diminishes the depth of this second dip in the spectrum, initially observed at θ=45° and d_{SiC}=300nm. At d_{SiC}=0 nm, no dips are present in the reflectance spectrum, indicating that the presence of both the metal and dielectric layers is essential for surface phonon-polariton excitation.

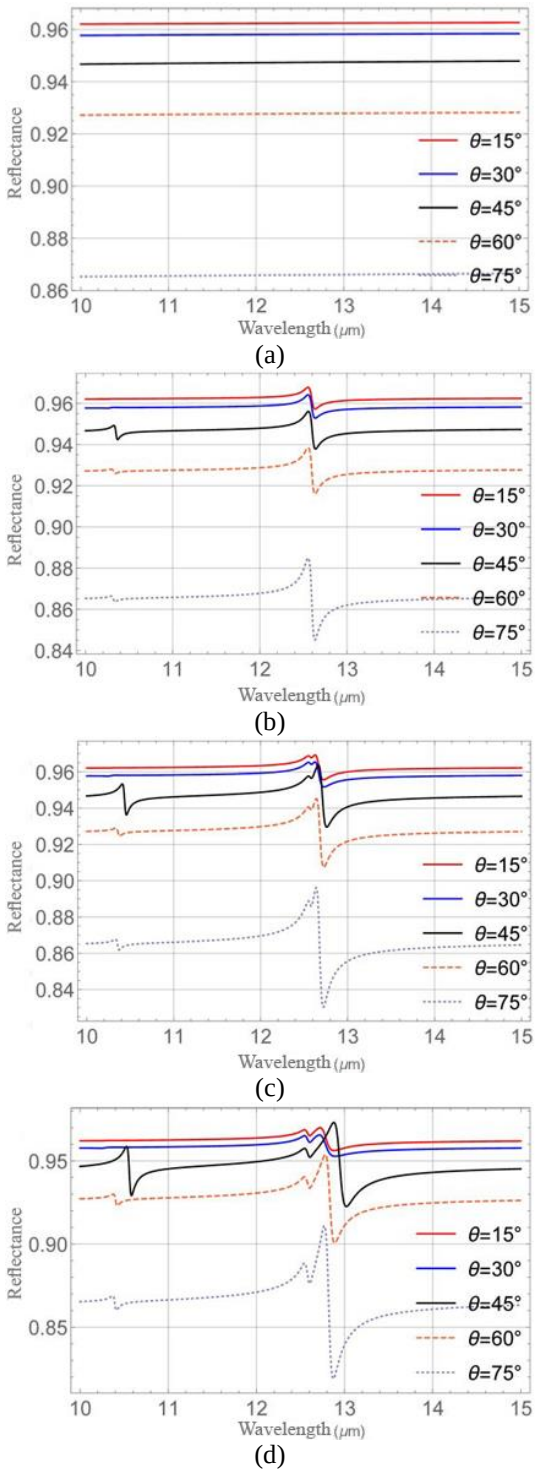

Fig. 15. Reflectance spectra of the metal and silicon carbide thin-layer structure and thickness of columnar silicon carbide thin film of (a) d_{sic}=0 nm, (b) d_{sic}=100 nm, (c) d_{sic}=200 nm, and (d) d_{sic}=300 nm.

VII. Conclusion

The excitation of surface phonon-polariton waves at the interface of a gold thin film and columnar silicon carbide thin film in the Kretschmann configuration was investigated, yielding the following findings:

The intensity of surface phonon-polariton wave excitation increases with increasing χ_v.

Excitation of surface phonon-polariton waves is impossible without either the metallic or dielectric layer. The presence of both layers is essential for the formation of the Reststrahlen band.

The optimal thickness for the gold layer in metal-dielectric structure is d_{met}=10 *nm*.

At a porosity of 0.8 in the silicon carbide thin film, the reflectivity spectra are entirely smooth and independent of variations in the thickness of the metallic or dielectric layers.

Increasing the thickness of columnar silicon carbide thin film enhances surface phonon-polariton wave excitation when the porosity is less than 0.6.

The optimal angle of incidence for the excitation of surface phonon-polariton waves is greater than 30°. No Reststrahlen band was observed at incidence angles of 15° and 30°.

The intensity of surface phonon-polariton wave in homogeneous and isotropic metal-dielectric structures is higher compared to heterogeneous metal-dielectric structures.

Acknowledgment

This work was carried out with the support of the University of Qom.

References

[1] A. Lakhtakia, "Surface-Plasmon waves at the planar interface of a metal film and a structurally chiral medium," Opt. Commun., Vol. 279, pp. 291–297, 2007.

[2] J. Polo, T. Mackay, and A. Lakhtakia, *Electromagnetic Surface Waves: A Modern Perspective*, Newnes, 2013.

[3] N. Rivera, T. Christensen, and P. Narang, "Phonon polaritonics in two-dimensional materials," Nano Lett., Vol. 19, No. 4, pp. 2653–2660, 2019.

[4] Q. Yan, D. Lu, Q. Chen, X. Luo, M. Xu, Z. Zhang, and P. Li, "Hybrid Ghost Phonon Polaritons in Thin-Film Heterostructure," Nano Lett., Vol. 24, No. 15, pp. 4346–4353, 2024.

[5] S.H. Hosseininezhad and F. Babaei, "Excitation of multiple surface plasmon-polaritons by a metal layer inserted in an equichiral sculptured thin film," Plasmonics, Vol. 13, No. 6, pp. 1867–1879, 2018.

[6] J.D. Caldwell, L. Lindsay, V. Giannini, I. Vurgaftman, T.L. Reinecke, S.A. Maier, and O.J. Glembocki, "Low-loss, infrared and terahertz nanophotonics using surface phonon polaritons," Nanophotonics, Vol. 4, No. 1, pp. 44–68, 2015.

[7] C.R. Gubbin, S. De Liberato, and T.G. Folland, "Surface phonon polaritons for infrared optoelectronics," J. Appl. Phys., Vol. 131, No. 3, pp. 030901(1-23), 2022.

[8] Y. Yang, *Phonon Polariton Enhanced Infrared Waveguides*, Ph.D. dissertation, Florida Institute of Technology, 2018.

[9] A.A. Alsalhin, M.F. Finch, and B.A. Lail, "Coupling between metallic structure and phonon polaritons for sensing applications," in Metamaterials, Metadevices, and Metasystems, SPIE, Vol. 10719, pp. 84–93, 2018.

[10] G. Lu, C.R. Gubbin, J.R. Nolen, T. Folland, M.J. Tadjer, S. De Liberato, and J.D. Caldwell, "Engineering the spectral and spatial dispersion of thermal emission via polariton–phonon strong coupling," Nano Lett., Vol. 21, No. 4, pp. 1831–1838, 2021.

[11] A. Fali, S.T. White, T.G. Folland, M. He, N.A. Aghamiri, S. Liu, J.H. Edgar, J.D. Caldwell, R.F. Haglund, and Y. Abate, "Refractive index-based control of hyperbolic phonon-polariton propagation," Nano Lett., Vol. 19, No. 11, pp. 7725–7734, 2019.

[12] X. Fang, J. Lou, Y.M. Chen, J. Wang, M. Xu, and K.C. Chuang, "Broadband Rayleigh wave attenuation utilizing an inertant seismic metamaterial," Int. J. Mech. Sci., Vol. 247, pp. 108182(1-14) ,2023

[13] T. Low, A. Chaves, J.D. Caldwell, A. Kumar, N.X. Fang, P. Avouris, and F. Koppens, "Polaritons in layered two-dimensional materials," Nature Mater., Vol. 16, No. 2, pp. 182–194, 2017.

[14] I. Pallikara, P. Kayastha, J.M. Skelton, and L.D. Whalley, "The physical significance of imaginary phonon modes in crystals," Electronic Structure, Vol. 4, pp. 033002(1-19), 2022.

[15] V. Dzhagan, A.P. Litvinchuk, M.Y. Valakh, and D.R. Zahn, "Phonon Raman spectroscopy of nanocrystalline multinary chalcogenides as a probe of complex lattice structures,". J. Phys.: Condensed Matter, Vol. 35, No. 10, pp. 103001(1-12), 2022.

[16] K. Parlinski and P. Piekarz, "Ab initio determination of Raman spectra of Mg_2SiO_4 and $Ca_2MgSi_2O_7$ showing mixed modes related to LO/TO splitting," J. Raman Spectroscopy, Vol. 52, No. 7, pp. 1346-1359, 2021.

[17] A.V. Zayats and I.I. Smolyaninov, "Optics of surface plasmon polaritons," J. Opt. A: Pure Appl. Opt., Vol. 5, No. 4, pp. 14-23, 2003

[18] L. Novotny and B. Hecht, *Principles of Nano-Optics*, Cambridge University Press, 2006.

[19] H.Zhu, Z. Xu, L. Cai, H. Wang, H. Luo, A. Pattanayak, P. Ghosh, M. Qiu, and Q.Li, "Ultrathin High Quality-Factor Planar Absorbers/Emitters Based on Uniaxial/Biaxial Anisotropic van der Waals Polar Crystals," Adv. Opt. Mater., Vol. 9, No. 21, pp. 2100645(1-9), 2021.

[20] S.Zhu, W. Zheng, X. Lu, L. Cheng, W. Zhong, and F. Huang, "Identification of TO and LO phonons in cubic natBP, 10BP and 11BP crystals," Appl. Phys. Lett., Vol. 118, No. 16, pp. 162106(1-5), 2021.

[21] F. Sizov, Z. Tsybrii, E. Rudenko, I. Korotash, M. Vuichyk, K. Svezhentsova, and D. Polotskiy, "Reststrahlen band infrared damping, microwave transparent AlN/polymeric film filters," Vacuum, Vol. 225, pp. 113248(1-12), 2024.

[22] A.V. Zayats, I.I. Smolyaninov, and A.A. Moradudin, "Nano-optics of surface plasmon polaritons," Phys. Rep., Vol. 408, pp. 131-314, 2005.

[23] H. Chul Kim and X. Cheng, "Infrared dipole antenna enhanced by surface phonon polariton," Opt. Soc. Am., Vol. 35, No. 22, pp. 3748-3750, 2010.

[24] M.D. Pickett, A. Lakhtakia, and J. Polo Jr, "Surface plasmon polaritons in metal films," Optik, Vol. 115, No. 9, pp. 393–398, 2004.

[25] A. Lakhtakia and R. Messier, "Sculptured Thin Films: Nanoengineered Morphology and Optics," SPIE, Vol. 143, 2005.

[26] H. Savaloni, F. Babaei, S. Song, and F. Placido, "Influence of substrate rotation speed on the nanostructure of sculptured Cu thin films," Vacuum, Vol. 85, No. 7, pp. 776-781, 2011.

[27] J. Yang, G.J. Brown, M. Dutta, and M.A. Stroscio,, "Photon absorption in the Restrahlen band of thin films of GaN and AlN: Two phonon effects," J. Appl. Phys., Vol. 98, No. 4, pp. 043517(1-5) , 2005.

[28] R. Chikkaraddy, A. Xomalis, L.A. Jakob, and J.J. Baumberg, "Mid-infrared-perturbed molecular vibrational signatures in plasmonic nanocavities," Light: Sci. Appl., Vol. 11, No. 1, pp. 19-27, 2022.

[29] G. Carini, R. Niemann, N.S. Mueller, M. Wolf, and A. Paarmann, "Surface phonon polariton ellipsometry," ACS Photon., Vol. 12, No. 2, pp. 792-800.,2025.

[30] D.T. Ha, D.T. Thuy, V.T. Hoa, T.T.T. Van, and N.A. Viet, "On the theory of three types of polaritons (Phonons, excitons, and plasmon polaritons)," J. Phys.: Conf. Ser., Vol. 865, pp. 012007(1-8), 2017.

[31] A.J. Huber, B. Deutsch, L. Novotny, and R. Hillenbrand, "Focusing of surface phonon polaritons," Appl. Phys. Lett., Vol. 92, No. 20, pp. 203104(1-3), 2008.

[32] S. Foteinopoulou, G.C.R. Devarapu, G.S. Subramania, S. Krishna, and D. Wasserman, "Phonon-polaritonics: enabling powerful capabilities for infrared photonics," Nanophoton., Vol. 8, No. 12, pp. 2129–2175, 2019.

[33] F. Babaei and H. Savaloni, "Numerical study of the remittances of axially excited chiral sculptured zirconia thin films," J. Modern Opt., Vol. 55, No. 12, pp. 1845-1857, 2008.

[34] F. Babaei, and H. Savaloni, "Reflection, transmission and circular dichroism in axially excited slab of a copper thin film helicoidal bianisotropic medium," Opt. Commun., Vol. 278, No. 2, pp. 321-328, 2007.

[35] J.A. Sherwin and A. Lakhtakia, "Nominal model for the optical response of a chiral sculptured thin film infiltrated by an isotropic chiral fluid-oblique incidence," Opt. Commun., Vol. 222, No. 1-6, pp. 305-329, 2003.

[36] J.A. Sherwin and A. Lakhtakia, "Nominal model for the optical response of a chiral sculptured thin film infiltrated with an isotropic chiral fluid," Opt. Commun., Vol. 214, No. 1-6, pp. 231-245, 2002.

[37] A. Lakhtakia, "On percolation and circular Bragg phenomenon in metallic, helicoidally periodic, sculptured thin films," Microwave Opt. Technol. Lett., Vol. 24, No. 4, pp. 239-244,2000.

[38] A. Lakhtakia, "Axial loading of a chiral sculptured thin film," Modelling Simulation Mater. Sci. Eng., Vol. 8, No. 5, pp. 677-687, 2000.

[39] J.A. Sherwin, A. Lakhtakia., and B. Michel, "Homogenization of similarly oriented, metallic, ellipsoidal inclusions using the Bruggeman formalism," Opt. Commun., Vol. 178, No. 4-6, pp. 267-273, 2000.

[40] F. Babaei and H. Savaloni, "On the dependence of circular Bragg phenomenon of noble metals helicoidally periodic sculptured thin films on visible and IR wavelengths," Opt. Commun., Vol. 278, No, 2, pp. 221-231, 2007.

[41] F. Babaei and M. Rostami, "Excitation of surface plexciton wave at interface of a metal and a columnar thin film infiltrated with J-aggregate dyes," Opt. Commun., Vol. 439, pp. 8-15, 2019.

[42] M. Rostami and F. Babaei, "Plexciton modes guided by an exciton slab in a columnar thin film," Optik, Vol. 268, pp. 169850(1-16), 2022.

[43] J.A. Polo, T.G. Mackay, and A. Lakhtakia, *Electromagnetic surface waves: a modern perspective*, Elsevier Insight, 2013.

Emadoddin Yaghooti was born in Qom on 1993. He received his PhD degree in condensed matter physics from University of Qom, Qom, Iran in 2025. He also completed his MSc and BSc degrees in Solid State Physics from University of Qom in 2016 and 2019, respectively. He has been teaching at Qom University for the past 6 years. His academic interests focus on plasmonics. He has published several papers on this subject in well-regarded domestic and international journals. He is a member of the Iranian Physics Society and was selected as a Distinguished Guest Lecturer at University of Qom in 2022.

Ferydon Babaei was born in Talesh on 1974. He received his PhD degree in optics of sculptured thin films from University of Tehran, Tehran, Iran in 2008. Then he joined the Department of Physics at University of Qom.

Now, he is an associate professor of condensed matter of physics. He studies the plasmonic properties and plasmon–exciton coupling in nanostructures and thin films. He has published more than 60 papers in international journals.